

Hydrodynamics, wall-slip, and normal-stress differences in rarefied granular Poiseuille flow

Ronak Gupta and Meheboob Alam*

Engineering Mechanics Unit, Jawaharlal Nehru Centre for Advanced Scientific Research, Jakkur PO, Bangalore 560064, India

(Received 12 December 2016; published 22 February 2017)

Hydrodynamic fields, macroscopic boundary conditions, and non-Newtonian rheology of the acceleration-driven Poiseuille flow of a dilute granular gas are probed using “direct simulation Monte Carlo” method for a range of Knudsen numbers (Kn , the ratio between the mean free path and the macroscopic length), spanning the rarefied regime of slip and transitional flows. It is shown that the “dissipation-induced clustering” (for $1 - e_n > 0$, where e_n is the restitution coefficient), leading to inhomogeneous density profiles along the transverse direction, competes with “rarefaction-induced declustering” (for $\text{Kn} > 0$) phenomenon, leaving seemingly “anomalous” footprints on several hydrodynamic and rheological quantities; one example is the well-known rarefaction-induced temperature bimodality, which could also result from inelastic dissipation that dominates in the continuum limit ($\text{Kn} \rightarrow 0$) as found recently [Alam *et al.*, *J. Fluid Mech.* **782**, 99 (2015)]. The simulation data on the slip velocity and the temperature slip are contrasted with well-established boundary conditions for molecular gases. A modified Maxwell-Navier-type boundary condition is found to hold in granular Poiseuille flow, with the velocity slip length following a power-law relation with Knudsen number Kn^δ , with $\delta \approx 0.95$, for $\text{Kn} \leq 0.1$. Transverse profiles of both first [$\mathcal{N}_1(y)$] and second [$\mathcal{N}_2(y)$] normal stress differences seem to correlate well with respective density profiles at small Kn ; their centerline values [$\mathcal{N}_1(0)$ and $\mathcal{N}_2(0)$] can be of “odd” sign with respect to their counterparts in molecular gases. The phase diagrams are constructed in the $(\text{Kn}, 1 - e_n)$ plane that demarcates the regions of influence of inelasticity and rarefaction, which compete with each other resulting in the sign change of both $\mathcal{N}_1(0)$ and $\mathcal{N}_2(0)$. The results on normal stress differences are rationalized via a comparison with a Burnett-order theory [Sela and Goldhirsch, *J. Fluid Mech.* **361**, 41 (1998)], which is able to predict their correct behavior at small values of the Knudsen number. Lastly, the Knudsen paradox and its dependence on inelasticity are analyzed and contrasted with related recent works.

DOI: [10.1103/PhysRevE.95.022903](https://doi.org/10.1103/PhysRevE.95.022903)**I. INTRODUCTION**

In the past few decades advances have been made in studying a system of suspended particles usually driven by a source of energy and interacting only via binary inelastic collisions. Under strong driving (say, via shaking or shear), the particles fly around randomly with large interparticle separation, analogous to a dilute molecular gas: such a dilute system of macroscopic particles is dubbed a *granular gas* [1–3]. The study of granular gases is interesting and challenging because of one important feature in which it differs from the traditional molecular gas: the constituent particles in a granular gas suffer *inelastic* collisions and hence lose energy via collisions. Besides being responsible for a wide variety of novel phenomena in granular gases, inelasticity also ensures spontaneous clustering of particles (density inhomogeneity) as well as the lack of scale separation [3]. We shall demonstrate in this work that the dissipation-induced clustering leaves seemingly “anomalous” footprints on several hydrodynamic and rheological quantities in granular Poiseuille flow. On the other hand, the issue of the separation of length and time scales is important if one has to rely on continuum formulations at the Navier-Stokes order. Using various theoretical, computational, and experimental approaches, a variety of prototypical flows of granular gases has been studied by many researchers [1–8].

The fluid confined between two walls and driven by a constant body force or pressure gradient (i.e., the Poiseuille flow) is a prototypical flow that has been of great interest

in the case of a molecular gas [9–17]; a schematic of an acceleration-driven Poiseuille flow is depicted in Fig. 1. While an incompressible flow admits a simple closed form solution for the Navier-Stokes equations, there is a characteristic departure from such continuum-level description in the case of a rarefied gas flow [18–22]. The nondimensional parameter Kn (Knudsen number) characterizes this departure, which includes unique features like (i) the bimodal shape [12,13] of the temperature profile (the “temperature-dip” or the “temperature-bimodality,” see the top-right panel in Fig. 1), (ii) the presence of a flow-rate minimum (the “Knudsen-minimum” or the “Knudsen-paradox” [9,10], see the bottom-right panel in Fig. 1), (iii) nonuniform pressure profile [13,15], (iv) normal stress differences [23–25], and (v) anomalous parallel heat flux [14,24,26]. The gravity-driven Poiseuille flow of a granular gas is a problem of interest due to the macroscopic size of the grains involved and the terrestrial gravity is strong enough to induce gradients on observable hydrodynamic quantities [27–34]. The grains flow between two parallel walls that are kept at a fixed temperature and as such can be imagined as thermal-walls [22,35] that allow us to study the bulk dynamics of the system. The cooling due to inelastic collisions is eventually balanced by the shear energy due to a constant body force, forcing the system into a nonequilibrium steady state that is analyzed for calculating hydrodynamic and rheological quantities [29–31]. Such gravity-driven granular flows are routinely encountered in chemical and processing industries, for example, in the riser section of fluidized bed reactors [27]. It must be noted, however, that the present problem of the Boltzmann limit of a granular gas undergoing Poiseuille flow is largely of academic

*meheboob@jncastr.ac.in

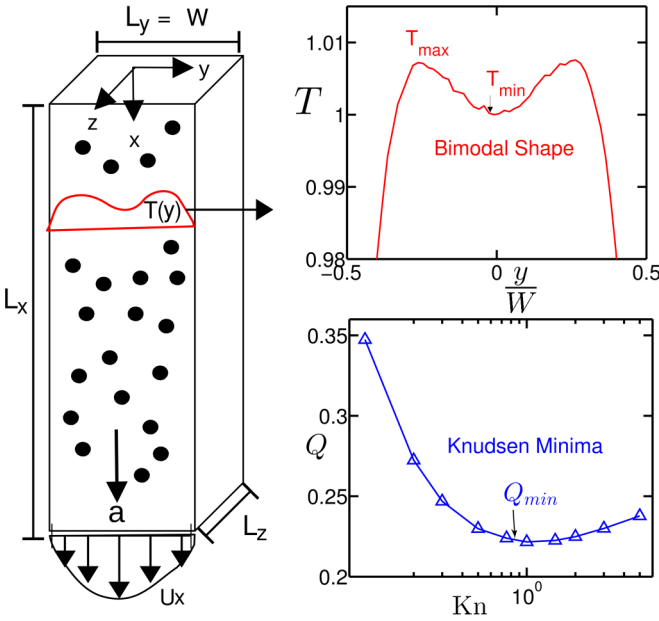


FIG. 1. Left: Schematic showing the acceleration-driven Poiseuille flow of hard spheres, with a representing the acceleration (directed along the x direction); two impenetrable-walls are placed at $y = \pm L_y/2$ and both x and z directions are periodic. Top-right: Typical temperature profile of “bimodal” shape having a local minimum at $y = 0$ and two maxima $T(y) = T_{\max}$ at $y = \pm y_s$. Bottom-right: Typical variation of the flow-rate, $Q = \int \rho(y)u_x(y)dy$, with Knudsen number Kn , with $Q = Q_{\min}$ (“Knudsen minimum”) at $\text{Kn} = O(1)$; here $\rho(y)$ and $u_x(y)$ represent the hydrodynamic profiles of the density and streamwise velocity, respectively, across the channel-width.

interest [18–22] from the viewpoint of developing and testing appropriate theoretical models [12,14–17,24–26,36] beyond Navier-Stokes-order.

The dilute granular Poiseuille flow has recently been tackled by one of us [34] using event-driven molecular dynamics (MD) simulations; however, only the hydrodynamic quantities (density, temperature, velocity, and the mass flow rate) were probed with a focus to understand the effects of inelastic dissipation on (i) the Knudsen paradox [9] and (ii) the bimodality [12] of the temperature profile; the rheology of dilute granular Poiseuille flow was not studied in Ref. [34]. It must also be noted that the boundary conditions in Ref. [34] were different (“nonthermal”) and hence a one-to-one comparison of Ref. [34] with the results for molecular gases was tentative. For example, it was found [34] that the degree of temperature bimodality increases with increasing inelastic dissipation, which is in contrast to the theoretical prediction [29] of its “nonmonotonic” variation; it was also speculated that axial inhomogeneities (which appear spontaneously in MD simulations of GPF) could be responsible for the disagreement between theory and simulation. Furthermore, it remained unresolved whether the “nonthermal” boundary conditions are in any way responsible for some of the observed behavior (e.g., the absence of the Knudsen-minimum effect for a wide range of parameters). In this work we employ the direct simulation Monte Carlo [37] (DSMC) method (see Sec. II), along with diffuse “thermal-wall” conditions, to simulate the

granular Poiseuille flow—the present simulation technique (DSMC) removes any ambiguity related to the first issue since the dissipation-induced axial-inhomogeneities are completely suppressed.

Three primary objectives of this work are to (i) reexamine the robustness of the dissipation-induced signatures of the hydrodynamic fields for a dilute granular Poiseuille flow as found in Ref. [34], (ii) examine the applicability of Maxwell-Navier-type boundary conditions for a dissipative or granular gas, and (iii) analyze the impacts of dissipation and rarefaction on its non-Newtonian rheology (normal stress differences, Sec. V). The rest of this paper is organized as follows. The microscopic boundary conditions and other simulation details are given in Sec. III. The results on (i) hydrodynamic fields, (ii) temperature bimodality, and (iii) macroscopic boundary conditions (Maxwell-Navier slip condition) are presented in Sec. IV. The issue of the presence or absence of the Knudsen-minimum in GPF and the role of the thermal and athermal nature of walls are discussed in Sec. VI—this settles a recently reported result [39] on Knudsen-paradox that apparently contradicts Ref. [34]. The summary and conclusions are presented in Sec. VII.

II. DIRECT SIMULATION MONTE CARLO METHOD

Here we provide a brief description of the DSMC method to solve the inelastic Boltzmann equation [37,38]; this is a particle-based “stochastic” algorithm that differs from the deterministic molecular dynamics (MD) methods. From kinetic theory we can estimate the number of collisions that occur in a dilute gas in a certain time step Δt in a certain volume V [37]:

$$N_c = \frac{2\pi R^2 N^2 \langle |v_{12}| \rangle \Delta t N_e}{V}. \quad (1)$$

In the above formula N is the number of simulated particles, R the particle radius, and v_{12} the relative velocity between two particles; in DSMC the number of simulation particles is not equal to the number of physical or real particles and the ratio is N_e , which appears in the above formula for choosing collision pairs. The number of simulated particles therefore only has a statistical significance and the number density of the simulated system can be arbitrarily increased without affecting the real density of the system; in present simulations we used $N = O(10^5)$.

The DSMC algorithm is designed to process N_c collisions in Eq. (1) using a certain “acceptance-rejection” scheme. Thus, we need to choose N_p number of pairs [37],

$$N_p = \frac{8\pi R^2 N^2 v_{12}^{\max} \Delta t N_e}{V}, \quad (2)$$

such that the number of accepted pairs is equal N_c as given in Eq. (1). A collision is accepted according to the following rule:

$$\Theta(\vec{k} \cdot \vec{v}_{12})|\vec{k} \cdot \vec{v}_{12}| > \text{rand}[0,1)v_{12}^{\max}, \quad (3)$$

where \vec{k} is an equidistributed random vector in three-dimensions. A bound on the parameter v_{12}^{\max} needs to be set for finding out the number of collision pairs to be chosen in a time step per cell; we set this parameter initially to three

times the most probable velocity and then dynamically update it. The above scheme, Eq. (3), ensures that the correct number of collisions occurs as predicted by the collision frequency derived from kinetic theory.

As an initial condition the particles are distributed randomly in the simulation domain that is divided into cells to process collisions; these cells should typically be a fraction of the mean free path. In the streaming stage the particle positions are updated and boundary conditions are applied for the relevant particles; the particles are subsequently sorted into cells depending on their positions. In the collision stage N_p pairs of particles are randomly chosen in each cell and if the collision is accepted the post-collision velocities are calculated according to the following collision rule:

$$\vec{v}_i = \vec{v}_i - \frac{1+e_n}{2} [(\vec{v}_i - \vec{v}_j) \cdot \vec{k}_{ij}] \vec{k}_{ij}, \quad (4)$$

$$\vec{v}_j = \vec{v}_j + \frac{1+e_n}{2} [(\vec{v}_i - \vec{v}_j) \cdot \vec{k}_{ij}] \vec{k}_{ij}. \quad (5)$$

Here e_n is the normal restitution coefficient and \vec{k}_{ij} is the unit vector along the line joining the centers of the colliding spheres; in DSMC [37] \vec{k}_{ij} is taken as a random vector \vec{k} that is equidistributed on a sphere in three dimensions. In all simulations we assume that the hard spheres are *smooth* and hence the tangential velocity of the colliding pair remains unchanged.

III. WALL CONDITIONS, AVERAGING, AND CODE VALIDATION

In order to simulate the body-force (such as gravity) driven Poiseuille flow, a constant acceleration of magnitude a is applied on every constituent particle (see the left panel in Fig. 1); the acceleration acts as a driving force that adds energy into the system. For the case of a molecular gas a steady state is facilitated by use of the “thermal-wall” boundary conditions; on the other hand, the granular gases have an inbuilt thermostat in the form of collisional cooling that ensures a steady state. For all simulations we distribute hard spheres of specified diameter (d) and mass (m), initialized with some random thermal velocity, inside the simulation domain as depicted in Fig. 1. The simulation domain is a cuboid of dimensions $L_x \times L_y \times L_z$, with two impenetrable walls placed at $y = \pm L_y/2$; the x and z directions are periodic. The particle-level boundary conditions are discussed next.

A. Thermal boundary conditions

The implementation of boundary conditions in DSMC is similar to MD since the simulation particles are treated as physical particles for the application of boundary conditions. Since the averaging cells are basically layers with nonunit dimension only in the direction perpendicular to the wall, the only relevant coordinate of the particle required for sorting is the y coordinate (see Fig. 1). The x and z coordinates of the particles are not updated or stored—the simulation domain is periodic in these two directions.

In the present work we model the walls as fully diffuse *thermal walls* [22,37] for which the walls are maintained at a fixed temperature T_w . For collisions with such thermal

walls, the x and z components of the velocity of a colliding particle forget their initial velocity and gain a post-collision velocity taken from a Gaussian distribution with variance corresponding to the temperature of the wall ($T_w = 1$) and a mean corresponding to the wall velocity, which in the present case is 0; on the other hand, the y component of the velocity is sampled from a “biased” Gaussian distribution and is reflected. To summarize, the post-collision velocity of a colliding particle with a wall is updated as follows:

$$v_x^{t+\Delta t} = \sqrt{\frac{k_B T_w}{m}} v_G + a t_{\text{post}}, \quad (6)$$

$$v_y^{t+\Delta t} = \sqrt{\frac{2k_B T_w}{m}} v_{\text{BG}}, \quad (7)$$

$$v_z^{t+\Delta t} = \sqrt{\frac{k_B T_w}{m}} v_G, \quad (8)$$

where v_G is the velocity sampled from a Gaussian distribution with zero mean and unit variance and v_{BG} is sampled from a biased-Gaussian distribution [38] (also known as Rayleigh probability distribution):

$$p(v_{\text{BG}}) = \frac{m|v_{\text{BG}}|}{k_B T_w} \exp\left(-\frac{m v_{\text{BG}}^2}{2k_B T_w}\right), \quad (9)$$

with the prefactor coming from the normalization condition $\int_0^\infty p(v_{\text{BG}}) dv_{\text{BG}} = 1$.

The x component of the velocity gets accelerated over the time it spends between the end of the time step and a collision with the wall (t_{post}). The increments in respective coordinates, x_{inc} , y_{inc} , and z_{inc} , for a particle-wall collision are then defined as

$$x_{\text{inc}} = v_x^t(t_{\text{pre}}) + \frac{a}{2} t_{\text{pre}}^2 + \sqrt{\frac{k_B T_w}{m}} v_G t_{\text{post}} + \frac{a}{2} t_{\text{post}}^2, \quad (10)$$

$$y_{\text{inc}} = v_y^t(t_{\text{pre}}) + v_y^{t+\Delta t} t_{\text{post}}, \quad (11)$$

$$z_{\text{inc}} = v_z^t(t_{\text{pre}}) + v_z^{t+\Delta t} t_{\text{post}}, \quad (12)$$

with t_{pre} and t_{post} denoting time pre- and post-collision, respectively.

B. Averaging procedure

After a certain time into the simulation when a steady state has been reached we begin averaging of hydrodynamic quantities, which are sampled after certain time steps and then time averaged. The statistical steady state of Poiseuille flow is ascertained by monitoring the constancy of the total energy of all particles [34]; this issue is discussed in the Appendix.

For the purpose of calculating macroscopic quantities, the entire simulation domain is partitioned into a number of *layers* or bins (of width δy), along the direction parallel to two impenetrable walls (see the left panel of Fig. 1). The layer-splitting instead of dividing the domain into cubic boxes is done because it is *a priori* known that the Poiseuille flow has gradients only along the y direction.

The macroscopic average of a particle-level quantity $\psi(\mathbf{v})$ is defined as:

$$\langle \psi(\mathbf{v}) \rangle_y = \frac{1}{N_t} \sum_t \frac{N_t}{V_{\text{bin}}} \sum_{i \in \text{bin}} \psi(\mathbf{v}_i(t)), \quad (13)$$

where \mathbf{v}_i is the velocity of i th particle and N_t is the number of time steps over which the quantity is sampled. The inner sum in Eq. (13) implies that this sum is taken over all particles residing in a bin which is centered at position y and the volume of the bin is $V_{\text{bin}} = \delta y L_x L_z$ (where δy is the width of the bin, and L_x and L_z are the lengths of the domain along x and z directions). By choosing appropriate form of $\psi(\mathbf{v})$ the relevant macroscopic and hydrodynamic fields are defined [13,14]:

$$\rho(y) = \langle m \rangle_y, \quad (14)$$

$$\mathbf{u}(y) = \frac{1}{\rho(y)} \langle m \mathbf{v} \rangle_y \equiv (u_x, u_y, u_z), \quad (15)$$

$$T(y) = \frac{m}{3k_B \rho(y)} \langle (\mathbf{v} - \mathbf{u})^2 \rangle_y, \quad (16)$$

as the density, the hydrodynamic velocity vector, and granular temperature, respectively.

C. Control parameters

To simulate a ‘‘dilute’’ granular gas, we set the average ‘‘reduced’’ density to $\rho_{\text{av}}^r \equiv n_{\text{av}} d^3 \leq 0.0121$ as in many previous studies on the Poiseuille flow of molecular gases [13,14]. There are three main control parameters in this problem: (i) the normal restitution coefficient e_n , (ii) the acceleration a , and (iii) the Knudsen number Kn , with the latter two being discussed below.

1. Forcing parameter: Dimensionless acceleration \hat{a}

The dimensionless acceleration \hat{a} is defined as

$$\hat{a} = \frac{aW}{\frac{2k_B T_w}{m}}, \quad (17)$$

where W is the channel width which measures the strength of the body force acting on a particle traveling a distance W . This implies that for $\text{Kn} = O(1)$ (and hence for $W \sim \lambda$) the dimensionless acceleration \hat{a} measures the strength of the body force between two successive collisions of particles. As such, \hat{a} can be thought of as a forcing parameter that is responsible for driving an initially homogenous system at equilibrium to an out-of-equilibrium state. A constant value of \hat{a} ensures that the system is subject to the same shear and allows us to make a proper dynamical comparison for various rheological quantities.

2. Knudsen number

The Knudsen number (Kn) measures the degree of rarefaction in the system and is the ratio of the mean free path and a characteristic length scale. The *global* Knudsen number is defined as

$$\text{Kn} = \frac{\lambda}{W}, \quad (18)$$

where $\lambda = (\sqrt{2}\pi n d^2)^{-1}$ is the equilibrium mean-free path of the system at $n = n_{\text{av}}$. For given channel dimension (W) and

average density (n_{av}), therefore, Kn is set as an input parameter for the simulations as it has been commonly used in previous studies [13,14] on the Poiseuille flow of molecular gases. To change Kn , two routes can be taken [34]: (i) vary the channel width keeping the number density and hence λ constant [this would require an adjustment of the value of a in each simulation to maintain the constancy of the parameter \hat{a} in Eq. (17)]; (ii) vary the number density keeping the channel width constant. The latter is more convenient since a single value of a will ensure the constancy of \hat{a} [see Eq. (17)] for all Kn .

We have used protocol (ii) for varying Kn in present simulations; the width of the channel is fixed at $W/d = 1860$ and the Knudsen number was varied via $\text{Kn} = (\sqrt{2}\pi n_{\text{av}} d^3)^{-1} / (W/d)$ for a range of reduced density $10^{-6} < \rho_{\text{av}}^r \equiv n_{\text{av}} d^3 \leq 1.21 \times 10^{-2}$; changing the channel width to $W/d = 5000$ did not affect the results as verified in present simulations. Note that a reduced density of $\rho_{\text{av}}^r = 1.21 \times 10^{-2}$ corresponds to an equilibrium mean free path of $\lambda = 186d$ [see Eq. (18)]. A few test cases were also carried out using protocol (i) and the results obtained are found to be identical for a given value of \hat{a} .

D. Bin width and the validation of DSMC code

1. Bin width

All the particles in a particular bin are used for averaging as described in Sec. III B. These bins or cells, also referred to as sampling cells, may or may not coincide with the cells used for computing collisions; in this paper, however, the sampling and collision cells are taken to be the same for almost all cases. Typically the bin size should be a fraction of the mean-free path; for present simulations, the width of the bin was varied between $\delta y = \lambda/3$ and $\lambda/200$, where λ is the equilibrium mean-free path, depending on the value of Kn and e_n . For example, at $\text{Kn} = 0.05$, a bin-width of $\delta y = \lambda/9$ (with 180 bins across the channel width) was found to be sufficient to yield resolved macroscopic fields for $e_n = 0.7$, while about 60 bins (i.e., $\delta y = \lambda/3$) yielded converged results for $e_n = 1$; at $\text{Kn} = 5$, a bin width of $\delta y = \lambda/200$ (40 bins across the channel width) was used, irrespective of the value of e_n . Care was taken while choosing the number of bins to simulate highly inelastic systems ($e_n \leq 0.7$) at small Knudsen number ($\text{Kn} < 0.1$) when the density becomes strongly inhomogeneous (along the transverse direction) for which a smaller bin width ($\delta y < \lambda/9$) is necessarily needed to resolve the macroscopic fields.

Note that the bin width can also affect the boundary values of hydrodynamic fields since a lesser bin width effectively measures a point closer to the wall than a bin with a larger width. In this regard, the data presented in Sec. IV C (wall-slip) were repeated with several choices of δy (especially at $\text{Kn} \sim 0$) till the bin-size independence of boundary values was found.

2. Code validation

We have tested our DSMC code by comparing the present results for the Poiseuille flow of a molecular gas with those obtained by Mansour *et al.* [13]. The dimensionless velocity and temperature profiles are shown in Figs. 2(a) and 2(b), respectively, for the case of $\hat{a} = 0.3$ and $\text{Kn} = 0.1$ with a reduced-density $\rho_{\text{av}}^r = n_{\text{av}} d^3 = 0.00121$; note that the velocity and temperature have been rescaled by $\sqrt{2k_B T_w / m}$

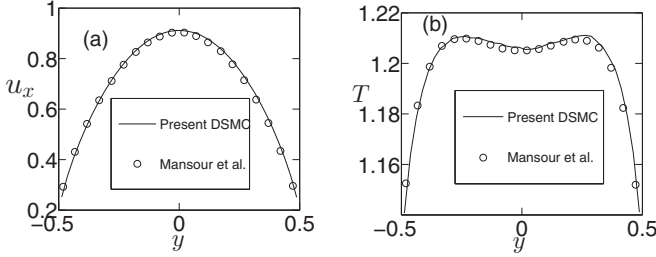


FIG. 2. Profiles of (a) streamwise velocity and (b) temperature and their comparisons with Mansour *et al.* [13] for a molecular gas at a Knudsen number of $\text{Kn} = 0.1$; the dimensionless acceleration is set to $\hat{a} = 0.3$ as in Ref. [13]. Note that the temperature has been rescaled by T_w and the velocity by $\sqrt{2k_B T_w/m}$.

and T_w , respectively. The bimodal-shape of the temperature profile [12], with a local minimum at $y = 0$ and two maxima away from the centreline, is clearly evident in Fig. 2(b); this will be further analyzed in Sec. IV B. Overall, there is a good quantitative match between our and Mansour *et al.*'s results for both fields, thereby validating the present DSMC code. Additional validation checks of this code are detailed in Sec. V (stress) and Sec. VI (Knudsen paradox).

IV. HYDRODYNAMIC FIELDS AND MAXWELL-NAVIER BOUNDARY CONDITION

For all simulations we fix the particle mass ($m = 1$), diameter ($d = 1$), Boltzmann constant ($k_B = 1$), and the wall temperature ($T_w = 1$) to unity; the simulation box is taken to be a cube with $L_x = L_y = L_z = W$. In the remaining part of this paper, the density is normalized by the average density ρ_{av} , the temperature is normalized by its wall value and the velocity is normalized by a characteristic velocity u_R :

$$\rho_R = \rho_{\text{av}}, \quad T_R = T_w, \quad u_R = \left(\frac{2k_B T_w}{m} \right)^{1/2}. \quad (19)$$

The transverse length has been normalized by W and hence $y \in (-0.5, 0.5)$ in all plots.

To analyze the effects of inelastic dissipation and rarefaction, the results are presented for a range of (i) restitution coefficient $e_n \in (0.5, 1)$ and (ii) Knudsen number $\text{Kn} \in (0.02, 10)$; however, the specific results are compared for four values of $e_n = (0.7, 0.9, 0.99, 1)$ and two values of $\text{Kn} = 0.05$ and 1. For all results in this section (hydrodynamics) as well as in Sec. V (stress), the dimensionless acceleration is set to $\hat{a} = 0.5$; the effect of varying \hat{a} is discussed in Sec. VI (and also in Fig. 8).

A. Profiles of density and Knudsen number

Figure 3 displays the density profiles for different values of the restitution coefficient e_n ; Figs. 3(a) and 3(b) correspond to data for two representative Knudsen numbers of $\text{Kn} = 0.05$ and 1, respectively. For perfectly elastic collisions ($e_n = 1$, red dot-dash line), the density profiles are convex upward (with density minimum located at the channel centerline $y = 0$), with mild density variation across the channel; the density profiles for nearly elastic collisions ($e_n = 0.99$, blue solid line) almost overlap with those for $e_n = 1$. With

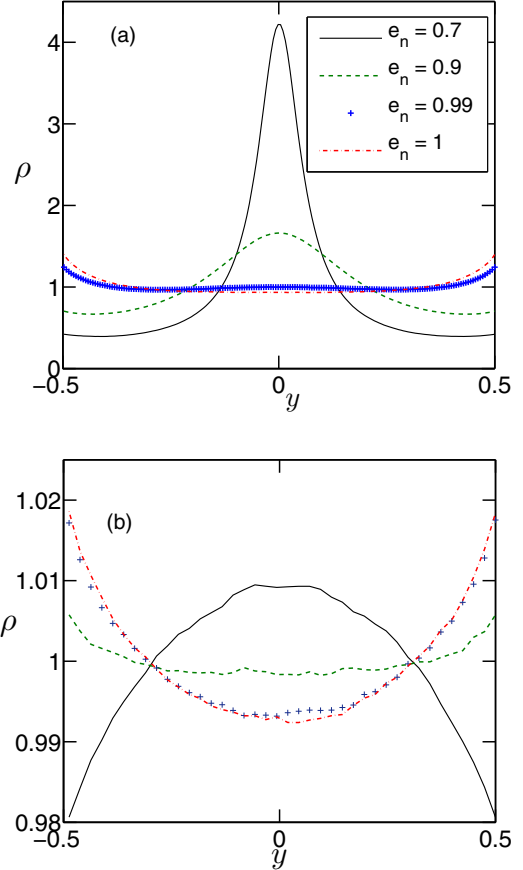


FIG. 3. Effect of restitution coefficient (e_n) on density profiles for (a) $\text{Kn} = 0.05$ and (b) $\text{Kn} = 1$; the dimensionless acceleration is $\hat{a} = 0.5$.

further increasing dissipations ($e_n = 0.9$ and 0.7), however, the density near the channel centerline increases and eventually the density-maximum occurs at the channel centerline $y = 0$ for sufficiently lower values of $e_n = 0.7$. The above qualitative observation holds for both small ($\text{Kn} = 0.05$, Fig. 3(a)) and large ($\text{Kn} = 1$) Knudsen number flows. It is noteworthy that for dissipative granular gases the density-maximum (at $y = 0$) can increase by several times the initial density at $\text{Kn} = 0.05$, but it remains very small at $\text{Kn} = 1$. The latter observation is indicative of the fact that the effects of inelasticity are suppressed in the rarefied regime where the wall-particle collisions are expectedly dominant.

Therefore, the granular Poiseuille flow exhibits a density inhomogeneity, which is characterized by a density peak at the center of the channel, in stark contrast to elastic and nearly elastic particles for which the density profiles are nearly homogenous. At small values of Kn , the particle-particle collisions dominate over particle-wall collisions and the particles tend to migrate to the low-shear region ($y = 0$), resulting in a density peak at $y = 0$ —this is due to the collisional-cooling mechanism [3] and hence dubbed “dissipation-induced clustering.” Moving from smaller to higher values of Kn for a granular gas ($e_n < 1$), the density again becomes uniform across the channel since the particle-wall collisions become the dominant mode of momentum transfer—this is dubbed “rarefaction-induced declustering” [34].

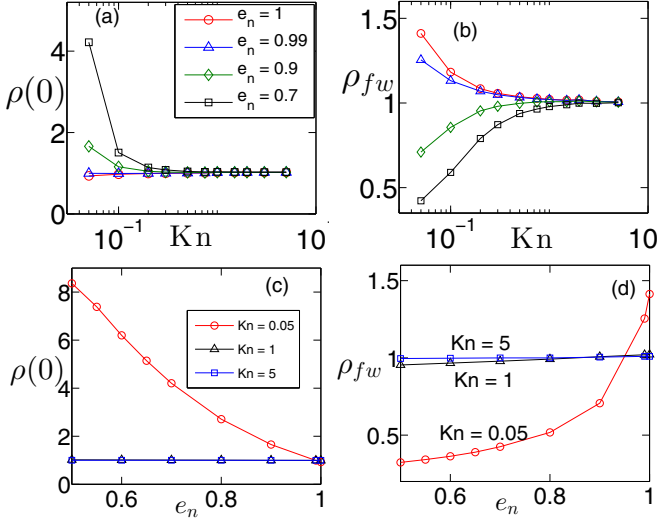


FIG. 4. Variations of (a) $\rho(0)$ and (b) ρ_{fw} with Knudsen number Kn for different e_n ; variations of (c) $\rho(0)$ and (d) ρ_{fw} with restitution coefficient e_n for different Kn . Other parameters are as described in the caption of Fig. 3.

The preceding discussion indicates that to fully characterize the density field we need to monitor two quantities: (i) the density field at the channel centerline $\rho(0)$ and (ii) its value near the wall,

$$\rho_{fw} = \frac{1}{2}[\rho(-0.5) + \rho(0.5)], \quad (20)$$

where the suffix “fw” denotes the density of the fluid adjacent to the walls. Figures 4(a) and 4(b) show the variations of $\rho(0)$ and ρ_{fw} with Kn for four different values of $e_n = 1$ (red circles), 0.99 (blue triangles), 0.9 (green diamonds), and 0.7 (black squares). It is seen that while for elastic and nearly elastic collisions ($e_n = 1$ and 0.99) the centerline (wall) density increases (decreases) slightly with increasing Kn , for dissipative collisions ($e_n = 0.9$ and 0.7) $\rho(0)$ and ρ_{fw} sharply decreases and increases, respectively, in the same limit; in either case both fields saturate to a near-constant value of 1, representing the average density of the system, for $Kn > 1$. The latter observation holds for any value of e_n , supporting the phenomenon of “rarefaction-induced declustering” [34] mentioned in the preceding paragraph. These overall findings are also evident in Figs. 4(c) and 4(d), which display the variations of $\rho(0)$ and ρ_{fw} with e_n for three values of $Kn = 0.05$ (red circles, representing near-continuum limit), 1 (black triangles) and 5 (blue squares): while there is no noticeable variations of $\rho(0)$ and ρ_{fw} with e_n in the rarefied regime ($Kn = 1, 5$), both fields vary significantly with decreasing e_n in the near-continuum limit of $Kn = 0.05$.

The density-variation (such as in Figs. 3 and 4) also affects the local mean-free path (and hence the local Knudsen-number) across the channel—this is shown in Fig. 5, with parameter values as in Fig. 3. The local Knudsen number is calculated from

$$Kn(y) = \frac{[\sqrt{2\pi}n(y)d^2]^{-1}}{W} \equiv Kn_y, \quad (21)$$

where $n(y)$ is the local binwise number density. The local Knudsen number for dissipative particles can be vastly

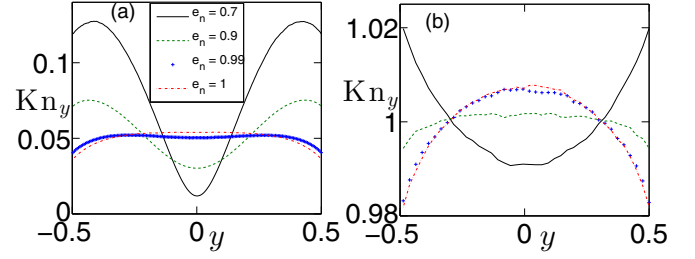


FIG. 5. Profiles of local Knudsen number Kn_y for different e_n : the global Knudsen number is (a) $Kn = 0.05$ and (b) $Kn = 1$. Other parameters are as described in the caption of Fig. 3.

different from its equilibrium preset value, especially for $Kn = 0.05$ [Fig. 5(a)], but its variation remains small at $Kn = 1$ for both elastic and granular particles, as seen in Fig. 5(b). On the whole, the amount of deviation of $Kn(y)$ from its equilibrium preset value depends on the transverse inhomogeneity in the density field, which is primarily dictated by inelastic dissipation in the near-continuum limit.

B. Bimodal temperature and its phase diagram

Figures 6(a) and 6(b) display the profiles of granular temperature, with the corresponding density fields in Figs. 3(a) and 3(b), respectively. From the equation of state ($p = \rho T$) in the low Kn regime, we can infer that the regions of high and

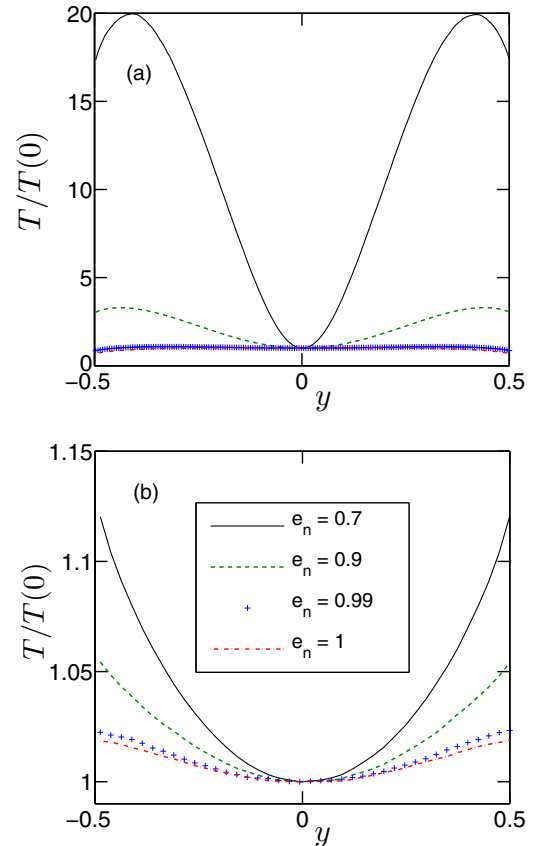


FIG. 6. Temperature profiles, $T/T(0)$, for (a) $Kn = 0.05$ and (b) $Kn = 1$. Parameter values are the same as described in the caption of Fig. 3.

low density will usually be accompanied by a region of low and high temperature, respectively; the (transverse) clustering of granular particles around the channel center [Fig. 3(a)] hence leads to the formation of a low-temperature region around $y = 0$ as it is evident in Fig. 6(a) for $e_n = 0.7$ (black solid line) and 0.9 (green dashed line). On the other hand, even for perfectly elastic collisions ($e_n = 1$), the temperature profile for a rarefied molecular gas undergoing Poiseuille flow is known to be of bimodal shape [12,13]: the channel-centerline corresponds to a local minimum of the temperature profile $T(y)$, with two symmetric maxima occurring at a few mean-free paths away from $y = 0$, see Fig. 2(b) for $\text{Kn} = 0.1$ —this was originally predicted by Tij and Santos [12] and verified later by Mansour *et al.* [13] via DSMC simulations. The present findings in Figs. 6(a) and 6(b) for $e_n = 1$ are similar to previous simulations of Ref. [13]; with increasing Kn [Fig. 6(b)] the location of the temperature-maxima shifts to the walls.

1. Phase diagram: Competition between dissipation and rarefaction

The phenomenon of temperature bimodality in the granular Poiseuille flow was recently investigated by Alam *et al.* [34] via MD simulations; they found that the origin of bimodality in a granular gas is tied to (i) inelastic dissipation as well as (ii) rarefaction, depending on the value of the Knudsen number. Another important finding from their study is that the temperature profiles always remain bimodal below a certain value of e_n (which is very close to 0.999). As mentioned in the Introduction (Sec. I) the boundary conditions in Ref. [34] are different (nonthermal) from present “thermal-wall” boundary conditions. In the following we reexamine the robustness of the related findings [34] of the bimodal-temperature profile in the granular Poiseuille flow with thermal walls.

To quantify the bimodal shape of the temperature profile, the following quantity is defined [34]:

$$\Delta T = \frac{T_{\max} - T(0)}{T(0)}, \quad (22)$$

dubbed *excess temperature* (i.e., the excess amount of maximum temperature within the flow with respect to its value at channel center $y = 0$). For a molecular gas, $\Delta T = 0$ as $\text{Kn} \rightarrow \text{Kn}_c \approx 0.02$ [34] and hence a nonzero value of $\Delta T > 0$ (that occurs for $\text{Kn} > 0$) is a signature of rarefaction effects. Overall, ΔT is a measure of the degree of temperature bimodality and a higher value of ΔT indicates a greater amount of bimodality in the temperature profile.

Figures 7(a) and 7(b) show the variations of the excess temperature ΔT with Kn and e_n , respectively. For the molecular gas [see the blue-diamond line in Fig. 7(a)] ΔT reduces on decreasing Kn , eventually vanishing in the limit of $\text{Kn} \rightarrow 0$ (at some small but finite value of $\text{Kn} = \text{Kn}_c \sim 0.03$)—therefore, the origin for temperature bimodality in a molecular gas is tied to rarefaction. At $e_n = 0.999$, the ΔT curve closely follows that for $e_n = 1$. However, further increasing inelasticity [$e_n = 0.995$ and 0.99, the green-squared and black-circled lines, respectively, in Fig. 7(a)] results in a *nonmonotonic* variation of ΔT with Kn , and the inelasticity now amplifies the excess-temperature at low $\text{Kn} \sim 0$. This “dissipation-induced”

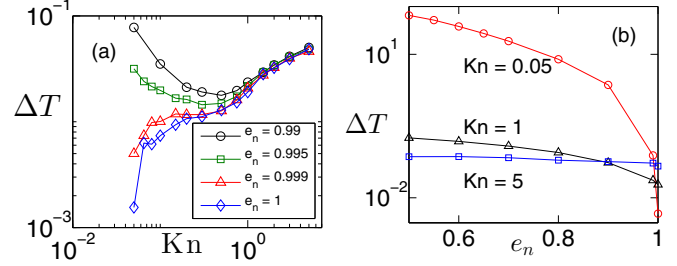


FIG. 7. Variations of excess temperature ΔT , Eq. (22), with (a) Knudsen number for different e_n and (b) restitution coefficient e_n for different Kn . Other parameters are as described in the caption of Fig. 6.

amplification of ΔT is more clearly evident in Fig. 7(b): while ΔT increases sharply with decreasing e_n at $\text{Kn} = 0.05$ (red-circled line), there is a much smaller increase of ΔT at $\text{Kn} = 1$ (black-triangled line) and an almost negligible change at $\text{Kn} = 5$ (blue-squared line which is nearly horizontal).

The above results indicate the presence of two mechanisms in causing the bimodal shape of the temperature profile: the inelastic dissipation is active at lower Kn and the rarefaction-effects kick in as we move to higher values of Kn . Based on a series of simulation-data for different e_n such as those in Fig. 7(a), a phase-diagram in the (Kn, e_n) plane, see Fig. 8, is constructed which demarcates two regions in which dissipation and rarefaction are independently dominant in causing temperature bimodality; the black circles on the phase boundary have been obtained by approximately determining at what value of Kn each ΔT curve for $e_n \neq 1$ coincides with that for $e_n = 1$ [see Fig. 7(a)]; note that this phase-boundary remains relatively insensitive to the value of dimensionless acceleration (see the filled triangles for $\hat{a} = 5$).

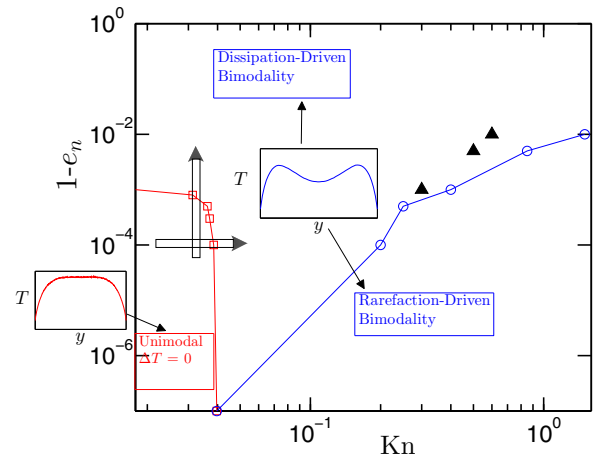


FIG. 8. Phase diagram of temperature bimodality in the $(\text{Kn}, 1 - e_n)$ plane for $\hat{a} = 0.5$; the black triangles represent data for $e_n = 0.99, 0.995, 0.999$ with $\hat{a} = 5$. The blue-circled line delineates the regions of (i) dissipation-driven and (ii) rarefaction-driven bimodal temperature profiles; the region to the left of red-squared line represents the region of “unimodal” temperature with $T_{\max} = T(0)$, i.e., $\Delta T = 0$. The “unimodal-to-bimodal” transition occurring along two arrows is ascertained in Fig. 9.

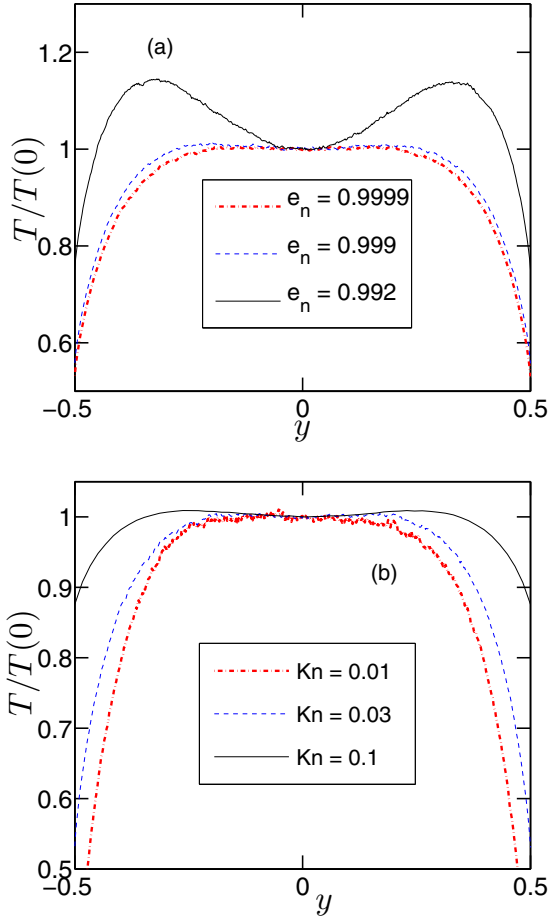


FIG. 9. “Unimodal-to-bimodal” transition of temperature profiles at (a) $\text{Kn} = 0.03$ (with increasing $1 - e_n$, i.e., “dissipation-driven” bimodality) and (b) $e_n = 0.9999$ (with increasing Kn , i.e., “rarefaction-driven” bimodality). In each panel, the temperature has been scaled by its centerline value; other parameters are as described in the caption of Fig. 8.

Around the bottom-left corner of Fig. 8 there is a very small region in which the temperature profile remains unimodal with $T_{\max} = T(0)$ (i.e., $\Delta T = 0$, marked as “Unimodal”); the red squares on the phase boundary enclosing the unimodal region were obtained by quadratically fitting the ΔT curves over $0.05 < \text{Kn} < 0.2$ for $e_n \geq 0.999$ [such as the two lower curves in Fig. 7(a)] and subsequently extrapolating each fitted curve to obtain the value of Kn at which $\Delta T = 0$. The “unimodal-to-bimodal” transition of temperature profiles is analyzed in Fig. 9: the profiles in Fig. 9(a) confirm the onset of this transition with increasing dissipation (and hence called “dissipation-driven” bimodality) and those in Fig. 9(b) with increasing rarefaction (and hence called “rarefaction-driven” bimodality).

2. Summary on temperature bimodality

The phase-diagram for temperature-bimodality in Fig. 8 looks strikingly similar to that in Fig. 8 of Alam *et al.* [34] who used “nonthermal” boundary conditions (in MD simulations of GPF)—we conclude that the walls being thermal or nonthermal does not affect the overall characteristics

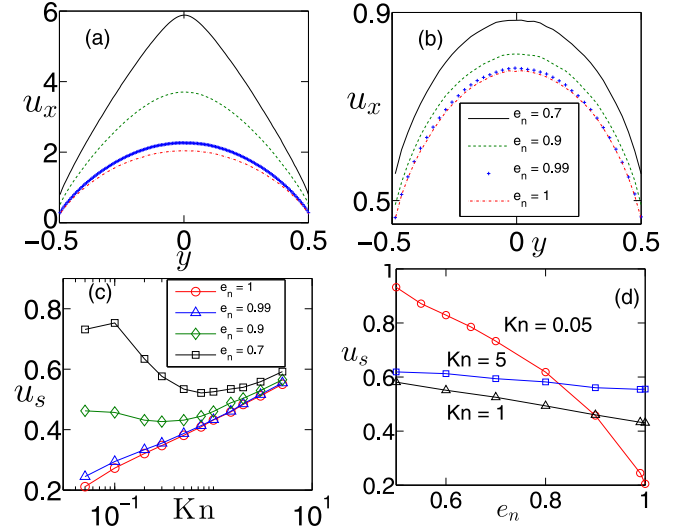


FIG. 10. (a), (b) Streamwise velocity profiles at (a) $\text{Kn} = 0.05$ and (b) $\text{Kn} = 1$ for different values of e_n . (c), (d) Variations of slip velocity with (c) Kn and (d) e_n for $\hat{a} = 0.5$.

of the temperature bimodality in granular Poiseuille flow. Moreover, the continual increase of the excess temperature ΔT with decreasing restitution coefficient [Fig. 7(b)] also agrees with results in Ref. [34]. On the whole, two different numerical techniques (MD and DSMC) and different boundary conditions (thermal and nonthermal) yield similar results for the temperature bimodality in a dilute granular Poiseuille flow. The present work therefore reconfirms the “unimodal-to-bimodal” transition scenario occurring as a consequence of the competition between rarefaction and dissipation [34].

C. Wall-slip: Velocity and temperature

In this section we analyze the role of inelastic dissipation on “wall-slip” phenomena (temperature-slip and velocity-slip at walls) and attempt to explain the related anomalous behavior (at small Knudsen numbers [34]) via Maxwell-Navier boundary conditions. Moreover, it is shown that a modified form of Maxwell-Navier slip condition holds for a granular gas.

1. Slip velocity and Maxwell-Navier boundary condition

The effect of inelasticity on streamwise velocity profiles are shown in Fig. 10 for (a) $\text{Kn} = 0.05$ and (b) $\text{Kn} = 1$. It is clear from Fig. 10(a) that for $\text{Kn} = 0.05$ the velocity profile deviates increasingly from a parabolic shape with increasing dissipation; see the black-solid and green-dash curves for $e_n = 0.7$ and 0.9 , respectively. There is a considerable amount of slip velocity (i.e., $u(\pm 1/2) \neq 0$) as seen in both panels of Figs. 10(a) and 10(b).

Since the walls are stationary, the slip velocity is calculated from

$$u_s = \frac{1}{2}[u_x(-0.5) + u_x(0.5)], \quad (23)$$

whose variations with Kn and e_n are shown in Figs. 10(c) and 10(d), respectively. In the limit of $\text{Kn} \rightarrow 0$ the velocity-slip vanishes for a molecular gas (assuming that the walls are

rough) and a finite slip occurs only at $\text{Kn} > 0$ and the velocity slip can thus be categorized as a rarefaction effect; this is seen in Fig. 10(c) where the red-circled line corresponding to $e_n = 1$ shows a monotonic increase of u_s with increasing Kn . However, the inelastic dissipation ($e_n < 0.99$) makes the variation of u_s with Kn *nonmonotonic*.

It must be noted that the nonmonotonic variation of slip velocity [viz. Fig. 10(a)] with Kn is distinctly different from the “monotonic” decrease of u_s with increasing Kn for $e_n < 0.9$ found by Alam *et al.* [34] (see their Fig. 5(a) which further shows that even for the case of $e_n = 1$ the slip velocity increases with increasing Kn but eventually decreases for $\text{Kn} > 2$, which was dubbed “anomalous” [34]). The above difference with the work of Alam *et al.* [34] could possibly be a consequence of the “nonthermal” boundary conditions employed in their work (see Sec. VI for a discussion on related issues).

The Kn -dependence of slip velocity in Fig. 10(c) is similar to what was reported more recently by Wu *et al.* [39]; the latter authors probed the same GPF (of a moderately dense system of inelastic hard disks) in contact with “thermal walls” by solving the Enskog-Boltzmann equation using a spectral method. In fact the decrease of slip velocity with increasing Kn in the low- Kn regime of GPF [Fig. 10(c)] is tied to the “dissipation-induced” clustering (rarefaction) of particles near the center (walls) of the channel. This issue can partially be explained (Wu *et al.* [39]) by considering the Maxwell-Navier slip boundary condition:

$$u_s \propto \frac{\text{Kn}}{\rho_{fw}} \left(\frac{du}{dy} \right)_{fw} \equiv \text{Kn}_{fw} \left(\frac{du}{dy} \right)_{fw}, \quad (24)$$

which is likely to be valid for $\text{Kn} < 0.1$. It is clear from Eq. (24) that the decrease of the near-wall density of the granular gas ρ_{fw} [Fig. 4(d)] with decreasing e_n would enhance the slip velocity in the same limit; the simulation data in Fig. 10(d) supports this finding.

To check the validity of Maxwell-Navier velocity-slip condition Eq. (24), we plot the variation of the dimensionless “velocity” slip length,

$$\zeta = \frac{u_s}{(du/dy)_{fw}}, \quad (25)$$

with local Knudsen number $\text{Kn}_{fw} = \text{Kn}/\rho_{fw}$ in Fig. 11(a); the variation of the velocity gradient at walls, $u'_w = (du/dy)_{fw}$, is displayed in Fig. 11(b). The inset of Fig. 11(a) indicates a good collapse of data for different $e_n \geq 0.9$. Focussing on the nearly elastic granular gas, the data for small Kn can be fitted via a power-law relation of the form

$$\zeta = \frac{u_s}{(du/dy)_{fw}} = \phi^{-1} \text{Kn}_{fw}^\delta, \quad (26)$$

where δ is the power-law exponent and ϕ is an effective specular coefficient [31]; the value of the exponent is $\delta \approx 0.96$ (for $\text{Kn}_{fw} \leq 0.1$). Therefore, the Navier’s slip condition [$u_s/u'_w \propto \text{Kn}_{fw}/\phi(\text{Kn}_{fw})$], with a weak Kn -dependent specular coefficient [$\phi(\text{Kn}) \sim \text{Kn}_{fw}^{0.04}$], holds in the quasielastic limit of a dilute granular gas for $\text{Kn} < 0.1$. A similar first-order boundary condition Eq. (26) was found to hold for a “dense” granular Poiseuille flow too, with a Kn -dependent specular coefficient [$\phi(\text{Kn}) \sim \text{Kn}^{1/8}$], as reported by Chikkadi and Alam [31].

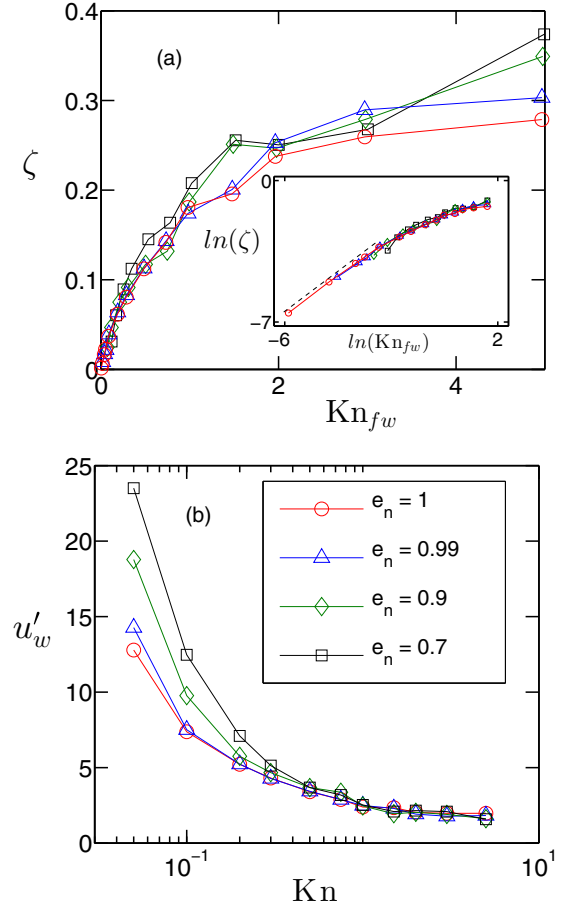


FIG. 11. (a) Validity of Maxwell-Navier velocity-slip condition: dimensionless slip-length $\zeta = u_s/u'_w$, Eq. (25), versus local Knudsen number Kn_{fw} in linear scale (main panel) and logarithmic scale (inset). (b) Variation of near-wall velocity gradient $u'_w = (du/dy)_{fw}$ with Kn for different e_n .

2. Temperature slip and its slip length

Figure 6 illustrates that the temperature profiles exhibit a slip as the fluid temperature near the wall (T_{fw}) is different from the preset wall temperature T_w . The temperature slip can be defined as

$$T_s = \frac{1}{2} [T(-0.5) + T(0.5)] - T_w \equiv T_{fw} - T_w, \quad (27)$$

where T_{fw} is the average temperature in the bins adjacent to two walls. Figures 12(a) and 12(b) show the variations of temperature slip with Knudsen number and restitution coefficient, respectively. It is seen from Fig. 12(a) that T_s follows a nonmonotonic trend with Kn : it first decreases and then increases with increasing Kn for any e_n ; the rate of decrease at small Kn increases sharply at $e_n = 0.9$ and 0.7 in comparison to nearly elastic systems ($e_n \geq 0.99$). As in the case of the velocity slip [viz. Fig. 10(c)], the T_s curves for all e_n in Fig. 12(a) merge together at sufficiently large values of Kn , implying that the bulk-dissipation does not influence the value of temperature slip in the rarefied regime of large Kn . The latter point is more evident in Fig. 12(b), which shows that while $T_s(e_n < 1) \approx T_s(e_n = 1)$ for a wide range of e_n at $\text{Kn} = 5$, the temperature slip T_s increases significantly with

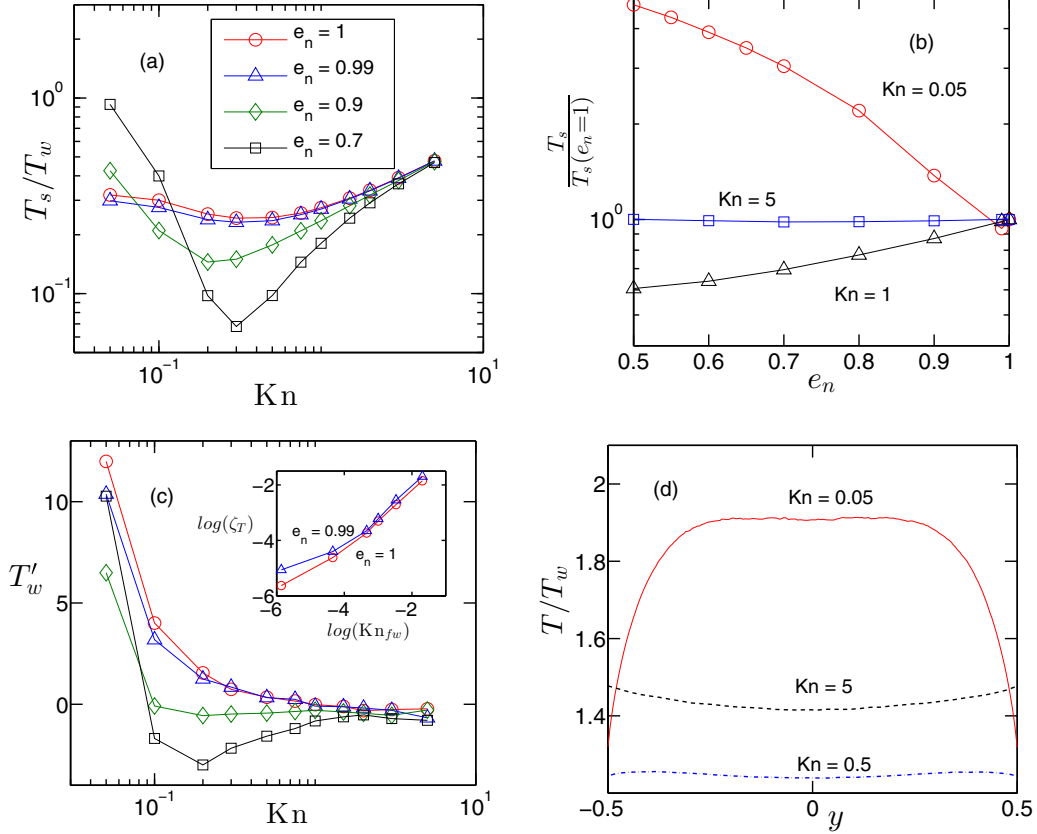


FIG. 12. (a), (b) Variations of temperature slip T_s , Eq. (27), with (a) Kn and (b) e_n ; in panel (b), T_s has been scaled by its value for $T_s(e_n = 1)$. (c) Variation of dimensionless $T'_w = (dT/dy)_{fw}$ with Kn for different e_n ; inset shows the variation of temperature slip-length ζ_T , Eq. (29), with local Knudsen number Kn_{fw} . (d) Temperature profiles for different Kn with $e_n = 1$, confirming the sign-change of T'_w with increasing Kn ; see text for details. Other parameters are as described in the caption of Fig. 11.

decreasing e_n in the limit of small Kn ($=0.05$) for which the bulk-dissipation due to inter-particle collision dominates over wall-particle collisions.

Figure 12(c) displays the variation of the temperature-gradient, $(dT/dy)_{fw}$, at wall with Knudsen number for different e_n . Unlike the positivity of the near-wall velocity gradient [viz. Fig. 11(b)], $(dT/dy)_{fw}$ undergoes a sign-reversal from positive to negative at some Kn irrespective of the value of the restitution coefficient—this sign change is tied to the temperature maximum being shifted continually toward the walls with increasing Kn as it is evident in Fig. 12(d). Note that the value of the critical Kn at which T'_w changes sign decreases with increasing dissipation (decreasing e_n). (This further reinforces the idea of dissipation-induced temperature bimodality as discussed in Fig. 8.)

From the well-known low- Kn relation [22] between the temperature slip and global Knudsen number (Kn),

$$T_s \propto \frac{\text{Kn}}{\rho_{fw}} \left(\frac{dT}{dy} \right)_{fw}, \quad (28)$$

where ρ_{fw} is the near-wall density of the gas, a slip length for the temperature can be defined as

$$\zeta_T = \frac{T_s}{(dT/dy)_{fw}}. \quad (29)$$

The variation of dimensionless ζ_T with local Knudsen number $\text{Kn}_{fw} \equiv \text{Kn}/\rho_{fw}$ is displayed in the inset of Fig. 12(c) for $e_n = 1$ and 0.99. Expectedly, the temperature slip-length ζ_T too increases with increasing Kn_{fw} , in agreement with Maxwell's boundary condition Eq. (28). Note that Eq. (28) must be modified to

$$T_s \propto c_1 \text{Kn}_{fw} \left(\frac{dT}{dy} \right)_{fw} + c_2 \text{Kn}_{fw} \left(\frac{d\rho}{dy} \right)_{fw} \quad (30)$$

in order to account for the Dufour-term (proportional to the density gradient), which is known to be a function of inelasticity ($1 - e_n$) and $c_2 = 0$ for $e_n = 1$. The nonoverlap of the slip-length data for $e_n = 0.99$ and 1 in the inset of Fig. 12(c) is presumably due to the increasing importance of the Dufour-contribution in the limit of $\text{Kn} \rightarrow 0$. A detailed analysis of the temperature boundary condition Eq. (30) for a granular gas and the determination of related exponents are left to a future work.

3. Summary on velocity and temperature slips

In summary, we found that the seemingly anomalous variations of both velocity [Fig. 10(c)] and temperature [Fig. 12(a)] slips for a granular gas at small Knudsen numbers can be explained from the related near-wall density variation of the gas with the restitution coefficient (which is tied to the transverse clustering of particles toward the channel center). A modified

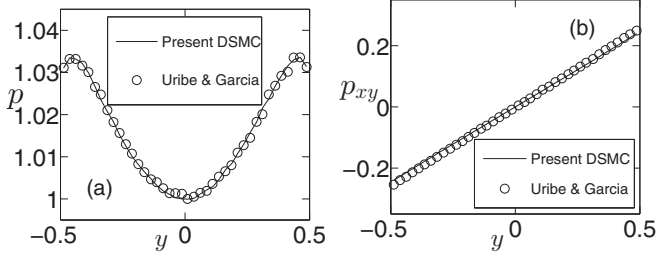


FIG. 13. Comparison between the present DSMC results (lines) with those of Uribe and Garcia (circles Ref. [14]) for (a) pressure $[p/p(0)]$ and (b) shear stress $[p_{xy}/p(0)]$ in the Poiseuille flow of a molecular gas at $\hat{a} = 0.3$ ($a = 0.00016$) and $\text{Kn} = 0.1$.

Maxwell-Navier boundary condition for “velocity” slip-length Eq. (26), with a Kn -dependent specular condition, holds for a dilute granular gas undergoing Poiseuille flow. Our data on temperature slip suggest that a Maxwell-type boundary condition, with appropriate modification for the Dufour-term Eq. (30), is likely to hold for the “temperature” slip length.

V. NONNEWTONIAN STRESS AND NORMAL STRESS DIFFERENCES

Here we analyze the stress tensor in a dilute granular Poiseuille flow, with the primary focus to understand the competing roles of inelasticity and rarefaction on two normal-stress differences. Attempt is also made to explain the simulation results via a comparison with the Burnett-order theory of Sela and Goldhirsch [23].

A. Stress tensor

In a dilute gas the stress tensor arises from the streaming motion of particles and is given by

$$\mathbf{P}_{\alpha\beta}(y) = \langle m(\mathbf{v}_\alpha - \mathbf{u}_\alpha)(\mathbf{v}_\beta - \mathbf{u}_\beta) \rangle_y = p\delta_{\alpha\beta} + \Pi_{\alpha\beta}, \quad (31)$$

where $p = (p_{xx} + p_{yy} + p_{zz})/3$ is the pressure and Π is the stress deviator; for the Poiseuille flow the only nonzero off-diagonal component is the shear stress p_{xy} , with $p_{yz} = 0 = p_{xz}$ (since there are no gradients along x and z directions and $u_y = 0 = u_z$; also verified in simulations). Figure 13 shows a comparison of the present data for pressure [Fig. 13(a)] and shear stress [Fig. 13(b)] with previous DSMC simulation of Uribe and Garcia [14] for $\text{Kn} = 0.1$, confirming the present calculations for the stress tensor components.

The effects of restitution coefficient on the transverse profiles for pressure and shear stress are displayed in Figs. 14(a)–14(d) for two values of the Knudsen number (a, c) $\text{Kn} = 0.05$ and (b, d) $\text{Kn} = 1$. Note that the stress tensor Eq. (31) has been normalized by $P_R = \rho_{av}U_R^2/2$ where $U_R = \sqrt{2k_B T_w/m}$ (except in Fig. 13). For a molecular gas the pressure profile is nearly uniform at $\text{Kn} \rightarrow 0$ [see red-dashed line in Fig. 13(a)] but varies considerably (with the pressure-minimum occurring at $y = 0$) at $\text{Kn} = 1$ [see Fig. 13(b)]. The underlying variations are due to rarefaction effects ($\text{Kn} > 0$) since at $\text{Kn} = 0$ the Navier-Stokes equations hold, which for steady Poiseuille flow

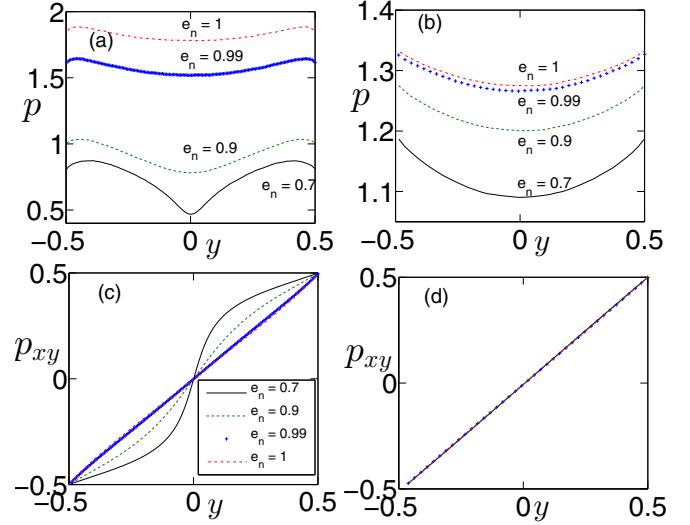


FIG. 14. Effects of dissipation (e_n) on the profiles of (a), (b) pressure and (c), (d) shear stress for (a), (c) $\text{Kn} = 0.05$ and (b), (d) $\text{Kn} = 1$. The dimensionless acceleration is $\hat{a} = 0.5$.

lead to (transverse momentum equation)

$$\frac{dp_{yy}}{dy} \equiv \frac{dp}{dy} = 0, \quad (32)$$

and consequently $p = p_{yy} = \text{constant}$. The deviation of the pressure profile from uniformity increases with increasing dissipation at $\text{Kn} = 0.05$ [see Fig. 13(a)], however, at $\text{Kn} = 1$ [Fig. 13(b)], the overall shape of the pressure profile remains relatively insensitive to varying e_n , which is due to the increasingly subdominant role of interparticle collisions (and hence of collisional dissipation) with increasing Kn . At any Kn the magnitude of pressure decreases with decreasing e_n which is tied to decreasing granular temperature in the same limit.

The streamwise momentum balance of Navier-Stokes equations for the Poiseuille flow leads to

$$\frac{dp_{xy}}{dy} = -\rho(y)a, \quad \Rightarrow \quad p_{xy} = a \int \rho(y)dy. \quad (33)$$

If the density is uniform (as is the case for both molecular and nearly elastic granular gases, see Fig. 3), the shear stress would vary linearly across the channel width as confirmed in Figs. 14(c) and 14(d). On the other hand, for dissipative particles ($e_n \ll 1$) at low- Kn , the density is significantly nonuniform [see Fig. 3(a)], resulting in increasingly more deviation of the shear stress from the linear profile as evident in Fig. 14(c).

B. Normal stress differences and comparison with theory

The diagonal components of the stress tensor Eq. (31) could be different from each other, leading to normal stress differences. The scaled first (\mathcal{N}_1) and second (\mathcal{N}_2) normal stress differences are defined via

$$\mathcal{N}_1 = \frac{p_{xx} - p_{yy}}{p}, \quad (34)$$

$$\mathcal{N}_2 = \frac{p_{yy} - p_{zz}}{p}, \quad (35)$$

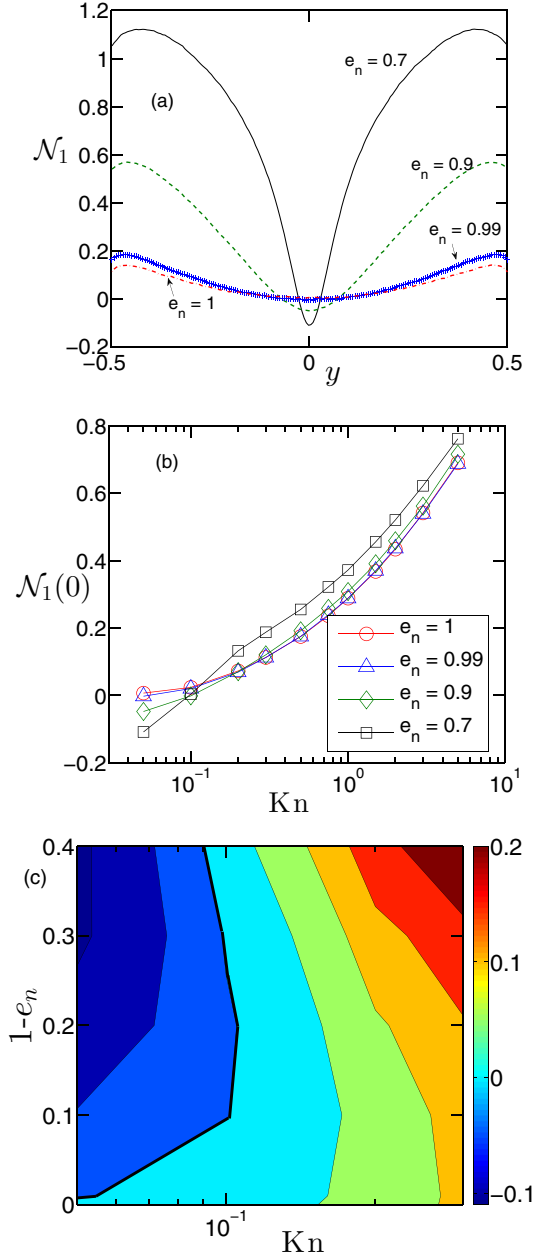


FIG. 15. (a) Effects of dissipation (e_n) on the profile of first [$\mathcal{N}_1(y)$] normal stress difference at $\text{Kn} = 0.05$; other parameters are as in Fig. 14. (b) Variations of the center-line value of $\mathcal{N}_1(0)$ with Kn for different e_n . (c) Phase diagram in the $(\text{Kn}, 1 - e_n)$ plane delineating the regions of positive and negative $\mathcal{N}_1(0)$; the thick black contour represents $\mathcal{N}_1(0) = 0$.

where each quantity is measured with respect to its mean isotropic pressure. The normal stress differences are indicators of the gas (fluid) being non-Newtonian (rarefied), since $\mathcal{N}_1 \approx 0 \approx \mathcal{N}_2$ for a Newtonian (nonrarefied) fluid [23].

1. First normal-stress difference

Figure 15(a) indicates considerable variations of the first normal stress difference across the channel width at $\text{Kn} = 0.05$. As in the cases of pressure and shear viscosity, \mathcal{N}_1

possesses relatively stronger spatial gradients at $\text{Kn} = 0.05$ [Fig. 15(a)] than at higher values of $\text{Kn} = 1$ (not shown); these gradients increase with increasing dissipation especially at lower values of Kn , with the latter being a consequence of dissipation-induced clustering (declustering) around the center (walls) of the channel.

It is noteworthy in Fig. 15(a) that the first normal stress difference remains positive at any Kn , except near the channel centerline (see the black line in Fig. 15(a) for $e_n = 0.7$). The above sign-reversal is clearly identified in Fig. 15(b), which shows the variations of $\mathcal{N}_1(0)$ with Kn for different e_n : $\mathcal{N}_1(0)$ becomes negative from positive at $\text{Kn} \leq 0.1$ for both $e_n = 0.9$ and 0.7 . Figure 15(c) displays the related phase-diagram in the $(\text{Kn}, 1 - e_n)$ plane delineating the regions of positive and negative $\mathcal{N}_1(0)$. It is clear that $\mathcal{N}_1(0)$ monotonically increases with increasing Kn at any e_n as expected in a rarefied gas.

2. Second normal-stress difference

The transverse profiles of the second normal stress difference $\mathcal{N}_2(y)$ for different e_n are displayed in Fig. 16(a) for a Knudsen number of $\text{Kn} = 0.05$. It is seen that $\mathcal{N}_2(y)$ can be positive or negative across the channel width, depending on the value of e_n and Kn . Figure 16(b) shows the variations of $\mathcal{N}_2(0)$ with Kn for different e_n . For elastic and nearly elastic ($e_n = 1, 0.99$) collisions, $\mathcal{N}_2(0) \approx 0$ at $\text{Kn} \rightarrow 0$, but its value decreases with increasing Kn , reaches a minimum (negative) and then increases again. A similar nonmonotonic behavior holds for $e_n = 0.9$ too, but $\mathcal{N}_2(0|e_n = 0.9) > 0$ and is maximum at $\text{Kn} \rightarrow 0$, reaches its minimum (negative) value at around $\text{Kn} \sim 1$, and then increases slowly toward zero. With further increasing dissipation to $e_n = 0.7$, $\mathcal{N}_2(0)$ decreases monotonically towards zero [see the black-squared line in Fig. 16(b)].

Figure 16(c) displays the contours of $\mathcal{N}_2(0)$, delineating its positive and negative values, in the $(\text{Kn}, 1 - e_n)$ plane—this should be contrasted with the related phase diagram of $\mathcal{N}_2(0)$ in Fig. 15(c). With increasing rarefaction (Kn), at any $e_n \neq 1$, while $\mathcal{N}_1(0)$ changes from negative to positive values at $\text{Kn} = \text{Kn}_1(e_n)$, $\mathcal{N}_2(0)$ changes from positive to negative values at $\text{Kn} = \text{Kn}_2(e_n)$. The locus of this critical Knudsen number $\text{Kn}_i(e_n)$ at which $\mathcal{N}_i(0)$ undergoes sign-reversal is denoted with a thick black contour in each phase diagram [Figs. 15(c) and 16(c)].

For a dilute granular gas under homogeneous shear [23–25,40–43] it is known that the first and second normal stress differences are positive and negative, respectively; these may be contrasted with the present results for Poiseuille flow on the respective center-line values of $\mathcal{N}_1(0)$ [Fig. 15(c)] and $\mathcal{N}_2(0)$ [Fig. 16(c)] at small values of Kn . In the following section we show that the present results are in tune with the Burnett-order theory of Sela and Goldhirsch [23].

3. Qualitative comparison with Burnett-order theory

To understand the sign-reversals of $\mathcal{N}_1(0)$ and $\mathcal{N}_2(0)$ with Kn , we analyze the leading-order expressions obtained from the Burnett-order theory of Sela and Goldhirsch [23]:

$$\mathcal{N}_1(0) = \delta_1 \text{Kn}_0^2 T''(0) + \delta_2 \text{Kn}_0^2 \rho''(0) / \rho(0) + \text{H.O.T.}, \quad (36)$$

where $T''(0) = d^2 T / dy^2 (y = 0)$, $\rho''(0) = d^2 \rho / dy^2 (y = 0)$ [note $T(0)$ and ρ_{av} have been used for normalization of

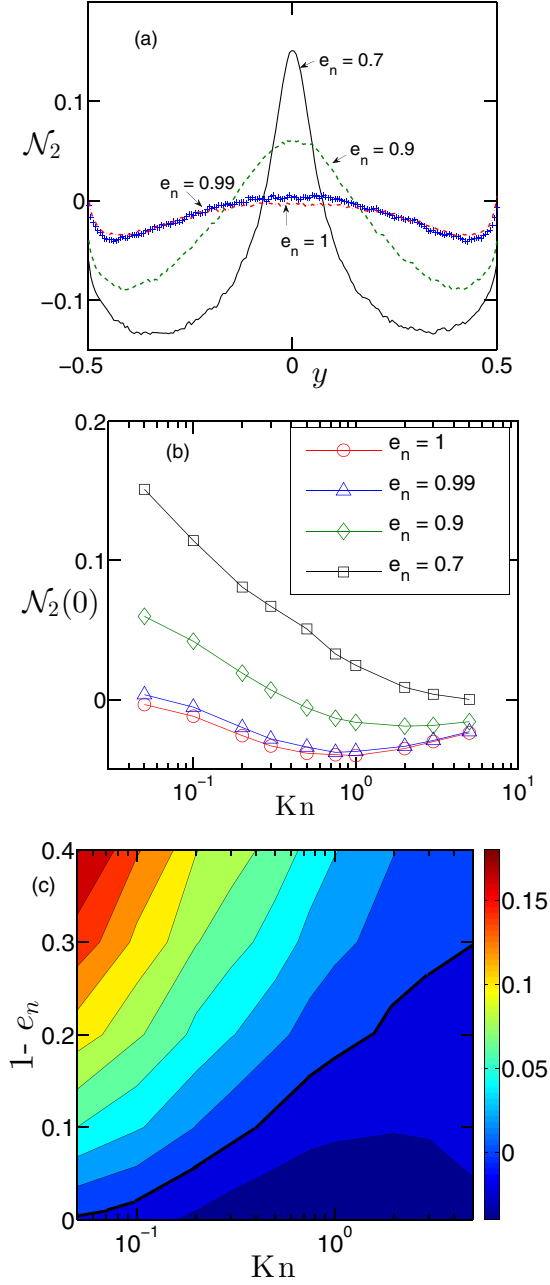


FIG. 16. (a) Effect of dissipation (e_n) on the profile of second (\mathcal{N}_2) normal-stress difference at $\text{Kn} = 0.05$; other parameters are as described in the caption of Fig. 14. (b) Variations of $\mathcal{N}_2(0)$ with Kn for different e_n . (c) Phase diagram in the $(\text{Kn}, 1 - e_n)$ plane delineating the regions of positive and negative $\mathcal{N}_2(0)$; the thick black contour represents $\mathcal{N}_2(0) = 0$.

temperature and density, respectively], and

$$\delta_1 = \frac{1}{3}\tilde{\omega}_2 - \tilde{\omega}_3 \approx -0.04, \quad \delta_2 = \frac{1}{3}\tilde{\omega}_2 \approx 0.214, \quad (37)$$

and $\text{Kn}_0 \equiv \text{Kn}(y = 0)$ is the local Knudsen number at the channel center; note that $\tilde{\omega}_i$'s in Eq. (37) are certain definite-integrals, related to the stress tensor at Burnett-order, which have been numerically evaluated in Ref. [23]. On the other hand, the leading expression for the second normal stress

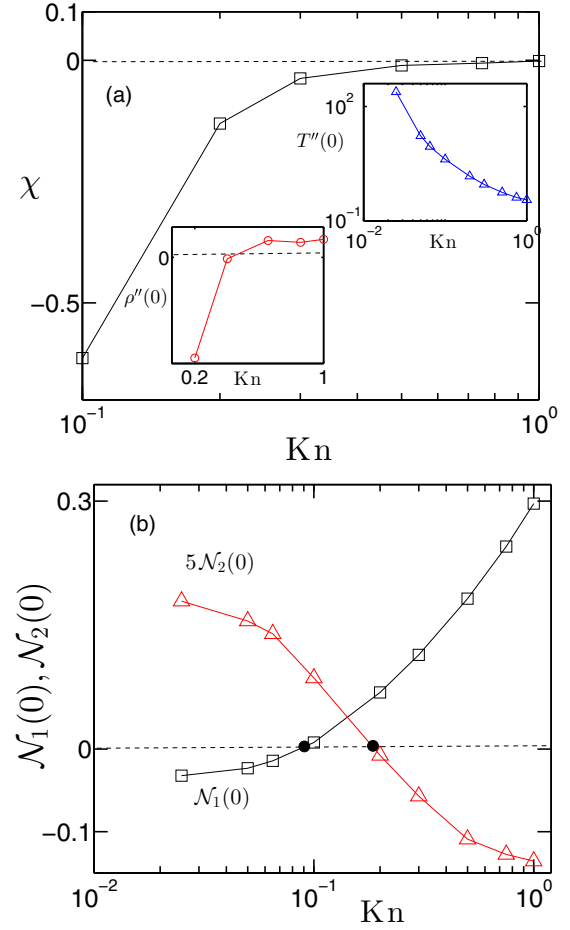


FIG. 17. (a) Variation of χ , Eq. (39), with Kn ; left and right insets show the corresponding variations of $\rho''(0)$ and $T''(0)$. (b) Variations of $\mathcal{N}_1(0)$ and $\mathcal{N}_2(0)$ with Kn . For all cases, $e_n = 0.95$ and $\hat{a} = 0.5$.

difference is [23]

$$\mathcal{N}_2(0) = -\mathcal{N}_1(0). \quad (38)$$

The latter prediction holds qualitatively in the regions of both small and large values of Kn ; see Figs. 16(c) and 15(c).

Given that $\delta_1 < 0$ and $\delta_2 > 0$, Eq. (36) indicates that the positive or negative value of $\mathcal{N}_1(0)$ depends on the signs of the second-derivatives of temperature and density; in particular, the sign reversal of the quantity

$$\chi(\text{Kn}) = \delta_1 T''(0) + \delta_2 \rho''(0)/\rho(0) \quad (39)$$

is directly tied to sign-reversal of both $\mathcal{N}_1(0)$ and $\mathcal{N}_2(0)$. Figure 17(a) displays the variation of Eq. (39) with Knudsen number for $e_n = 0.95$ [with $T''(0)$ and $\rho''(0)$ obtained from simulation data; see insets in Fig. 17(a)]; the corresponding variations in Fig. 17(b) of both $\mathcal{N}_1(0)$ and $\mathcal{N}_2(0)$ indicate its sign-reversal at $\text{Kn}_1 = 0.1$ and $\text{Kn}_2 \approx 0.2$, respectively. For this parameter combination, the curvature of the temperature profile remains positive for the range of Kn shown [see the right inset in Fig. 17(a)]; this implies that the temperature-profile has a minimum at the channel center (which corroborates well with the phase-diagram in Fig. 8). On the other hand, the curvature of the density profile [the left inset in Fig. 17(a)] changes

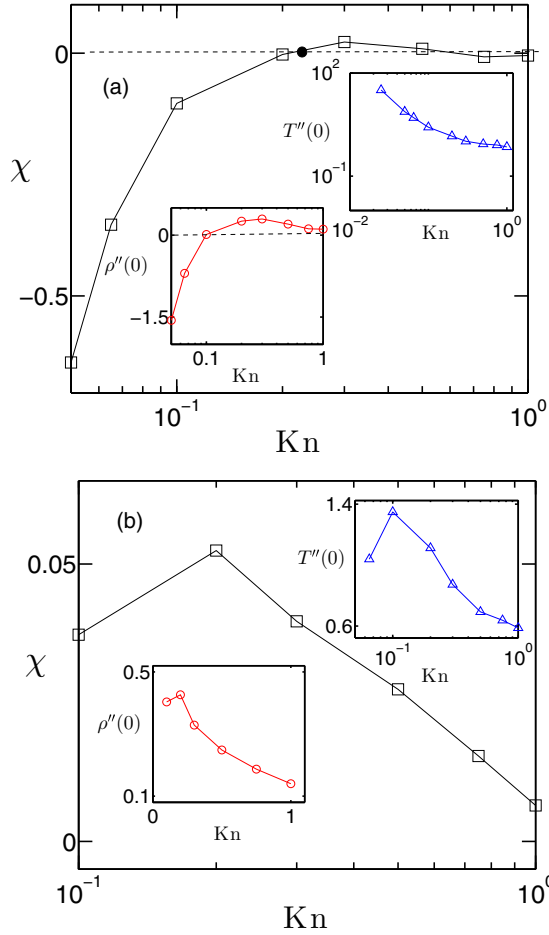


FIG. 18. Same as Fig. 17(a), but for (a) $e_n = 0.99$ and (b) $e_n = 1$.

sign from negative (concave down) to positive (convex up) at $\text{Kn} \sim 0.3$.

While Fig. 17(a) confirmed that χ remains negative for the range of Kn shown, the sign-change of χ is indeed captured by theory at $e_n = 0.99$; see the main panel of Fig. 18(a). However, this sign change occurs at a much larger value of $\text{Kn} \approx 0.25$ than the sign change of corresponding simulation data for $-\mathcal{N}_2(0)$ [see the blue-triangled line in Fig. 16(b)]. At $e_n = 1$, χ remains positive for all Kn as seen Fig. 18(b), having the same sign of the corresponding $\mathcal{N}_1(0)$ and $-\mathcal{N}_2(0)$ [see Figs. 15(b), 15(c), 16(b), and 16(c)]. On the whole, the Burnett-theory [23] yields correct variation of both $\mathcal{N}_1(0)$ and $\mathcal{N}_2(0)$ at small Kn , but is unable to predict their sign-change at large Kn (except in the quasielastic limit $e_n \geq 0.99$).

The main panels of Figs. 17(a) and 18(a) confirm that the same-sign correlation between theory [χ , Eqs. (39) and (36)] and simulation [$\mathcal{N}_1(0)$ and $-\mathcal{N}_2(0)$] holds only at small values of Kn for $e_n < 1$. The inadequacy of Sela and Goldhirsch [23] theory at large Kn for an inelastic gas ($e_n < 1$) may be attributed to two factors: (i) this theory is based on Burnett-order corrections [$O(\text{Kn}^2)$ and $O(\epsilon^2)$, with $\epsilon = 1 - e_n$] and hence is likely to be valid only for small values of Kn and ϵ ; (ii) the wall-particle collisions are likely to dominate the bulk-rheology of Poiseuille flow at large Kn , but the above theory is designed for “unbounded” shear-flow devoid of any wall-effect. The latter point suggests that the related

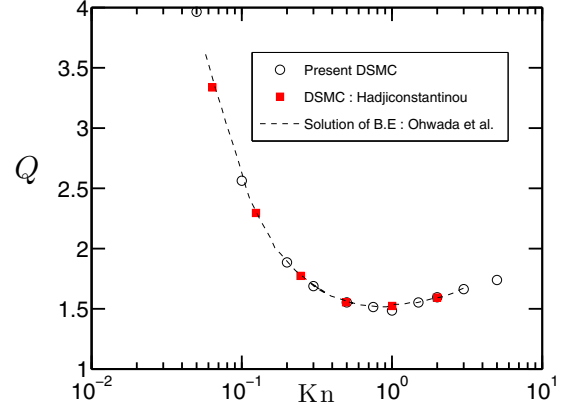


FIG. 19. Nondimensional mass-flow rate vs. Knudsen number in the Poiseuille flow of a molecular gas. The circles and filled squares denote results from present DSMC code (with $\hat{a} = 0.5$) and Ref. [16], respectively; the dashed line is the numerical solution of the Boltzmann equation (Ohwada *et al.* [11]) taken from Fig. 2 of Ref. [16].

boundary-value problem for Poiseuille flow, with appropriate boundary conditions for higher-order fields, needs to be solved to further probe the range of validity of this theory. On the whole, based on present comparisons, it appears that this theory is valid for a small range of $(\text{Kn}, 1 - e_n) \sim 0$.

VI. KNUDSEN PARADOX AND THE ROLE OF INELASTICITY

The nonmonotonic variation of the mass-flow rate with the Knudsen number (see Fig. 19) in the Poiseuille flow of a molecular gas, dubbed the “Knudsen paradox” or the “Knudsen-minimum” effect, was discovered by Knudsen [9] while measuring the mass-flow rate of noble gases flowing through a microcapillary; a theoretical explanation of this paradox was offered much later by Cercignani and Daneri [10] from the asymptotic solution of the Boltzmann-BGK equation. In Fig. 19 the dimensionless mass-flow rate, calculated from

$$Q = \frac{\int_{-W/2}^{W/2} \rho(y) u_x(y) dy}{\rho_{\text{av}} \sqrt{\frac{2k_B T_w}{m}} W \hat{a}}, \quad (40)$$

has been compared with those taken from Hadjiconstantinou [16] and the numerical solution of the Boltzmann equation [11]; the quantitative agreement between simulation and theory is excellent and a minimum in the flow rate is found at $\text{Kn} \sim O(1)$.

When the inelastic dissipation is taken into account, we find that the Knudsen minimum survives as illustrated in Fig. 20. It is seen that the flow rate for any e_n decreases steeply with Kn , reaches a minimum at $\text{Kn} \sim 1$, and increases thereafter with further increasing Kn ; the inset in Fig. 20(a) indicates that the Knudsen number at which Q_{min} occurs is pushed toward a higher value of Kn with increasing inelasticity. On the other hand, the flow rate at lower values of Kn increases with decreasing e_n due to the enhanced bulk velocity aided by density clustering around the channel center as explained previously by Alam *et al.* [34]. These overall findings hold

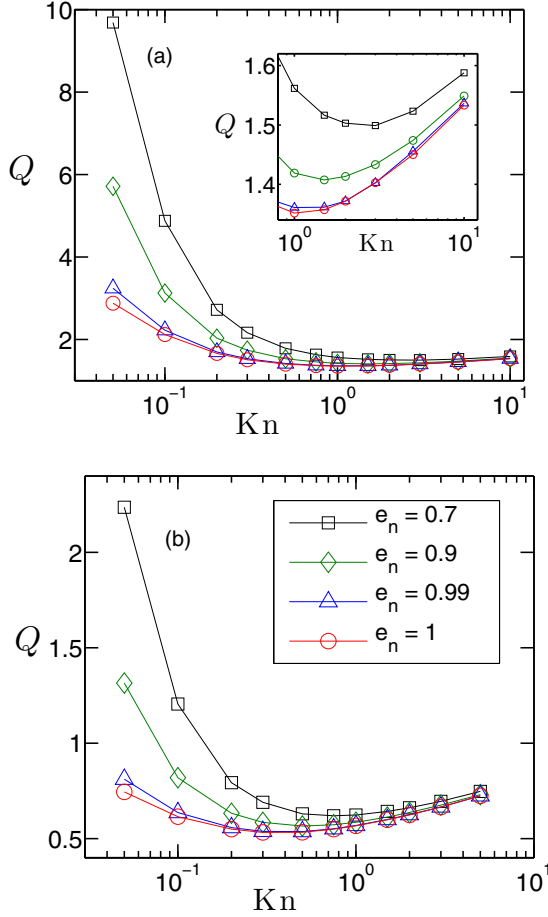


FIG. 20. Variations of the flow rate with Knudsen number for different e_n for dimensionless accelerations of (a) $\hat{a} = 0.5$ and (b) $\hat{a} = 10$. The inset in panel (a) is a zoom of its large Kn variation.

at other values of the forcing parameter; see Fig. 20(b) for $\hat{a} = 10$.

All results presented so far are based on “fully-diffuse” thermal-wall conditions—we have also carried out simulations with “partially-diffuse” walls [with the accommodation coefficient $\alpha \in (0, 1)$, with $\alpha = 1$ and 0 referring to fully diffuse and fully specular collisions [22], respectively]. The flow-rate variation looks similar to those in Fig. 20, irrespective of the particle-wall collisions being specular or diffuse. Therefore, the Knudsen paradox is present in a granular gas undergoing Poiseuille flow in contact with both diffuse and specular thermal walls.

The present results in Fig. 20 are in agreement with the recent work of Wu *et al.* [39], which reported the presence of Knudsen minima in the GPF in contact with thermal walls as used in the current simulations; note that the latter work [39] solved the underlying Enskog-Boltzmann equation via a spectral method. In contrast, the presence of Knudsen minimum in Fig. 20 for any e_n (and at arbitrary \hat{a}) is at odds with the results of Alam *et al.* [34], who found that (i) the Knudsen minimum is absent for a granular gas (except for very smooth walls and nearly elastic particles), and (ii) the flow-rate at sufficiently large values of Kn decreases for both smooth and rough walls. These differences are clearly due to

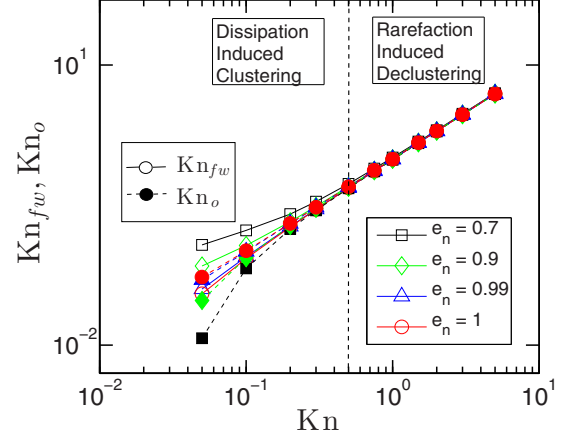


FIG. 21. Dissipation-dominated and rarefaction-dominated regimes in the $(\text{Kn}, \text{Kn}_0/\text{Kn}_{fw})$ plane. In a dissipation-dominated regime the “local” Knudsen numbers [Kn_0 (filled symbols) and Kn_{fw} (open symbols) that correspond to the gas-densities at the centerline and walls, respectively, of the channel] are different from “global” Knudsen number (Kn , based on preset mean density).

the “nonthermal” boundary conditions adopted in Ref. [34], although the underlying mechanistic reasons remain unclear at present.

Collectively, the present work along with Refs. [34,39] point toward the crucial role played by the nature (thermal or nonthermal) of the walls in determining the behavior of the bulk quantities (like the mass-flow rate, slip velocity, etc.) in the rarefied regime of the Poiseuille flow. How the nonthermal nature of walls could affect the mass-flow rate as well as the rheological quantities is left for a future work.

VII. SUMMARY AND OUTLOOK

The DSMC method was used to investigate (i) the hydrodynamic fields, (ii) the slip-length, and (iii) the non-Newtonian rheology (normal stress differences) in the acceleration-driven flow of a dilute granular gas through a vertical channel; the results were presented for a range of Knudsen numbers ($0.03 \leq \text{Kn} < 10$) spanning the rarefied regimes of slip and transitional flows. It was shown that the dissipation-induced clustering (leading to inhomogeneous density profiles along the transverse direction) competes with rarefaction-induced ($\text{Kn} > 0$) declustering phenomenon, leaving certain “anomalous” footprints on several hydrodynamic and rheological quantities; one example of such anomalous behavior is the well-known rarefaction-induced temperature bimodality [12], which could also result from inelastic dissipation in the continuum limit ($\text{Kn} \rightarrow 0$) as uncovered recently by one of us [34]. Figure 21 approximately demarcates two regimes: (i) $\text{Kn} < \text{Kn}_c \sim 0.5$ (dissipation-induced clustering dominates) and (ii) $\text{Kn} > \text{Kn}_c$ (rarefaction dominates over inelastic dissipation). Note that the circles represent the case of a molecular gas ($e_n = 1$) that follow a 45° line for which the global (Kn) and local ($\text{Kn}_0, \text{Kn}_{fw}$) Knudsen numbers are nearly equal. It is clear from this figure that $\text{Kn}_{fw} > \text{Kn}_0$ in the low- Kn regime, and this inequality becomes stronger with both (a) increasing inelastic dissipation and (b) decreasing Kn (for any $e_n < 1$),

a consequence of dissipation-induced transverse clustering becoming increasingly stronger in the same limit.

A. Hydrodynamics and boundary condition

We found that the present “thermal-wall” and the previously adopted “nonthermal” [34] boundary conditions have significant impact on the Knudsen paradox phenomenon (Sec. VI), but the characteristics of the temperature bimodality (Sec. IV B) are relatively insensitive to the type of wall-conditions employed. Overall, the present work reconfirmed the “unimodal-to-bimodal” transition scenario occurring as a consequence of the competition between rarefaction and dissipation [34].

Our results on the dependence of the excess temperature ΔT [Eq. (22) and Fig. 7(b)] on restitution coefficient are in agreement with what has been found previously [34] in MD simulations of the same problem (but with “nonthermal” walls). However, both the present and the previous [34] results on ΔT are in contrast to theoretical predictions of Tij and Santos [29]: “ ΔT decreases with decreasing e_n up to some value of $e_n \approx 0.5$ and subsequently increases with further decrease in e_n .” The latter discrepancy might be due to the stochastic-heating scheme incorporated in the theoretical analyses of Ref. [29].

The seemingly anomalous variations of both slip-velocity [Fig. 10(c)] and temperature-slip [Fig. 12(a)] in the low Knudsen-number regime have been explained from the related near-wall density variation of the gas with the restitution coefficient [Fig. 4]—the latter results from increasing degree of transverse clustering of particles (toward the channel center) with increasing dissipation. It is shown that a modified Maxwell-Navier slip-velocity condition [Eq. (26)], with a Kn-dependent specularity condition, holds for a dilute granular gas undergoing Poiseuille flow. The increasing importance of the Dufour term in the temperature-slip condition [Eq. (30)] is demonstrated in the low-Kn regime; the related issues are left for a future work.

B. Normal stress differences and the Burnett-order theory

The results on the transverse profiles of the pressure, shear stress, and the first (\mathcal{N}_1) and second (\mathcal{N}_2) normal-stress differences were discussed in Sec. V. An additional dissipation-driven effect uncovered here was that both the normal stress differences at channel center [$\mathcal{N}_1(0)$ and $\mathcal{N}_2(0)$] can be of “odd” sign with respect to their counterparts in molecular gases. The phase-diagrams were constructed in the $(\text{Kn}, 1 - e_n)$ plane that demarcates the regions of influence of inelasticity and rarefaction, which compete with each other resulting in the sign change of both $\mathcal{N}_1(0)$ and $\mathcal{N}_2(0)$. It was shown that the Burnett-order theory of Sela and Goldhirsch [23] can explain the behavior of both normal stress differences at small values of Kn and $(1 - e_n)$; however, this theory seems to have a limited range of validity in terms of inelasticity since it is unable to predict the sign change of $\mathcal{N}_1(0)$ and $\mathcal{N}_2(0)$ for larger inelasticities ($1 - e_n > 0.01$).

The phase-diagrams in Figs. 15(c) and 16(c) reinforce the increasing importance of both normal stress differences with increasing dissipation even in the limit of small Knudsen number. [The Navier-Stokes-order theory holds for $\text{Kn} \rightarrow 0$,

but in the presence of inelastic dissipation one must also put an additional constraint of $e_n \rightarrow 1$.] This, together with the phase-diagram for temperature bimodality in Fig. 8 (whose origin has been tied to super-Burnett order terms [12]), clearly calls for higher-order theories to correctly model the dynamics of a driven-granular gas undergoing Poiseuille flow. All presented results on the hydrodynamic fields and the stress tensor would be useful to validate such (higher-order)

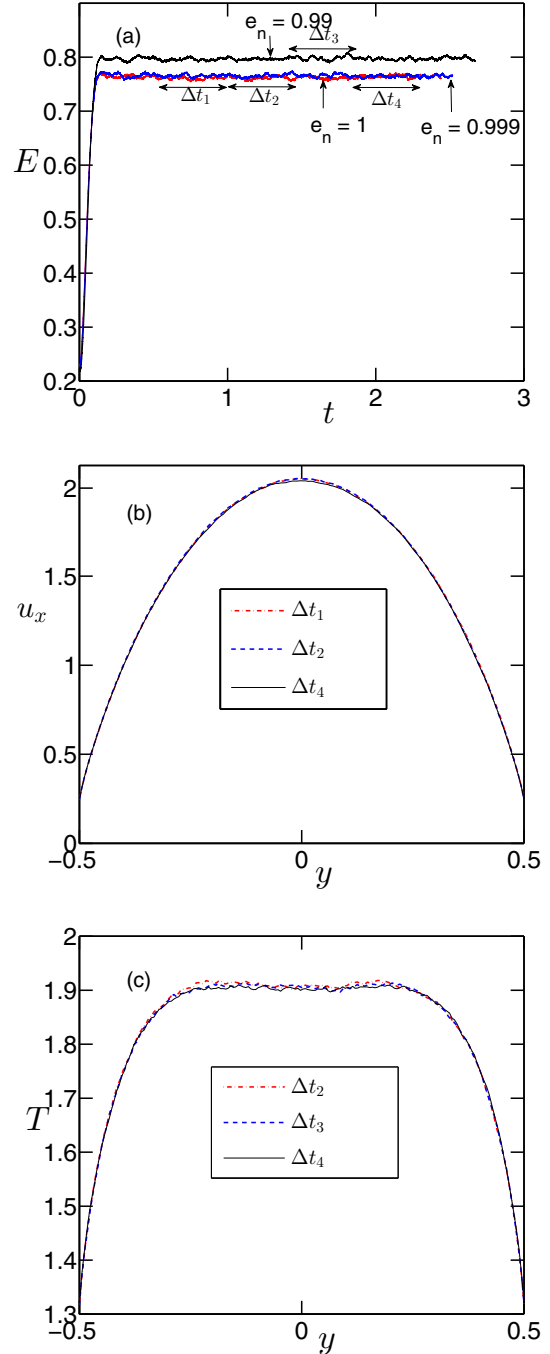


FIG. 22. (a) Temporal evolution of total kinetic energy, $E = \sum_i m v_i^2 / 2$ ($\times 10^{-5}$), of all particles for $\text{Kn} = 0.05$ and $\hat{a} = 0.5$; the time axis is scaled as $t \times 10^5$. (b) Streamwise velocity and (c) temperature (T/T_w) profiles, averaged over different time windows for $e_n = 1$.

constitutive models for rarefied granular gases—this can be done by solving the Burnett-order equations [23–25,36,43] with appropriate boundary conditions for Poiseuille flow.

APPENDIX: STATISTICAL STEADY STATE OF POISEUILLE FLOW

To check whether the present system of acceleration-driven Poiseuille flow has reached a statistical steady state or not, we monitor the total energy of all particles,

$$E(t) = \frac{1}{2} \sum_i m v_i^2, \quad (\text{A1})$$

as depicted in Fig. 22(a) for three different values of the restitution coefficient; the Knudsen number is $\text{Kn} = 0.05$ and the walls are modeled as fully diffuse thermal walls as

discussed in Sec. III A. It is seen that the energy saturates to a constant value for both elastic ($e_n = 1$) and inelastic ($e_n < 1$) particles.

For the purpose of calculating macroscopic and hydrodynamic fields, typically the averaging is carried out over 10^5 snapshots after the attainment of constancy of energy. To validate this procedure, we calculated velocity and temperature profiles over different time windows in the statistical steady state as shown in Figs. 22(b) and 22(c). Figure 22(b) displays three velocity profiles that were calculated by averaging over three different time windows of Δt_1 , Δt_2 , and Δt_4 as marked in Fig. 22(a); all three profiles collapse with each other. Similarly, the temperature profiles calculated over Δt_2 , Δt_3 , and Δt_4 are displayed in Fig. 22(c); note that to estimate the peculiar velocity in each case we have used the macroscopic velocity calculated over Δt_1 . It is seen that the temperature profiles at later times (Δt_3 and Δt_4) collapse well compared to the one over Δt_2 (within the bulk), although the differences are very minor.

-
- [1] C. S. Campbell, Rapid granular flows, *Annu. Rev. Fluid Mech.* **22**, 57 (1990).
 - [2] T. Pöschel and S. Luding, *Granular Gases* (Springer, Heidelberg, 2001).
 - [3] I. Goldhirsch, Rapid granular flows, *Annu. Rev. Fluid Mech.* **35**, 267 (2003).
 - [4] J. T. Jenkins and M. W. Richmann, Kinetic theory of plane flows of a dense gas of identical, rough, inelastic, circular disks, *Phys. Fluids* **28**, 3485 (1985).
 - [5] J. J. Brey, J. W. Dufty, C. S. Kim, and A. Santos, Hydrodynamics for granular flow at low density, *Phys. Rev. E* **58**, 4638 (1998).
 - [6] J. M. Montanero, V. Garzo, M. Alam, and S. Luding, Rheology of two- and three-dimensional granular mixtures under uniform shear flow: Enskog kinetic theory versus molecular dynamics simulations, *Granul. Matt.* **8**, 103 (2006).
 - [7] V. Garzo, A. S. Santos, and J. M. Montanero, Modified Sonine approximation for the Navier-Stokes transport coefficients of a granular gas, *Physica A* **376**, 94 (2007).
 - [8] N. V. Brilliantov and T. Pöschel, *Kinetic Theory of Granular Gases* (Oxford University Press, Oxford, 2004).
 - [9] M. Knudsen, Die Gesetze der Molekularströmung und der inneren Reibungsströmung der Gase durch Röhren, *Ann. Phys.* **28**, 75 (1909).
 - [10] C. Cercignani and A. Daneri, Flow of a rarefied gas between two parallel plates, *J. Appl. Phys.* **34**, 3509 (1963).
 - [11] T. Ohwada, Y. Sone, and K. Aoki, Numerical analysis of the Poiseuille and thermal transpiration flows between two parallel plates on the basis of the Boltzmann equation for hard-sphere molecules, *Phys. Fluids A* **1**, 2042 (1989).
 - [12] M. Tij and A. Santos, Perturbation analysis of a stationary nonequilibrium flow generated by external force, *J. Stat. Phys.* **76**, 1399 (1994).
 - [13] M. M. Mansour, F. Baras, and A. L. Garcia, On the validity of hydrodynamics in plane Poiseuille flows, *Physica A* **240**, 255 (1997).
 - [14] F. J. Uribe and A. L. Garcia, Burnett description of plane Poiseuille flow, *Phys. Rev. E* **60**, 4063 (1999).
 - [15] K. Aoki, S. Takata, and T. Nakanishi, Poiseuille-type flow of a rarefied gas between two parallel plates driven by a uniform external force, *Phys. Rev. E* **65**, 026315 (2002).
 - [16] N. G. Hadjiconstantinou, Dissipation in small scale gaseous flows, *ASME J. Heat Trans.* **125**, 944 (2003).
 - [17] P. Taheri, M. Torrilhon, and H. Struchtrup, Couette and Poiseuille microflows: Analytical solutions for regularized 13-moment equations, *Phys. Fluids* **21**, 017102 (2009).
 - [18] J. C. Maxwell, On stresses in rarefied gases arising from inequalities of temperature, *Philos. Trans. R. Soc. London* **170**, 231 (1879).
 - [19] D. Burnett, The distribution velocities in a slightly nonuniform gas, *Proc. Lond. Math. Soc.* **39**, 385 (1935).
 - [20] H. Grad, On the kinetic theory of rarefied gases, *Commun. Pure Appl. Maths.* **2**, 331 (1949).
 - [21] M. N. Kogan, *Rarefied Gas Dynamics* (Plenum Press, New York, 1969).
 - [22] C. Cercignani, *Rarefied Gas Dynamics* (Cambridge University Press, Cambridge, 2000).
 - [23] N. Sela and I. Goldhirsch, Hydrodynamic equations for rapid flows of smooth inelastic spheres, upto Burnett order, *J. Fluid Mech.* **361**, 41 (1998).
 - [24] S. Saha and M. Alam, Non-Newtonian stress, collisional dissipation and heat flux in the shear flow of inelastic disks: A reduction via Grad's moment method, *J. Fluid Mech.* **757**, 251 (2014).
 - [25] S. Saha and M. Alam, Normal stress differences, their origin and constitutive relations for a sheared granular fluid, *J. Fluid Mech.* **795**, 549 (2016).
 - [26] M. Alam and S. Saha, Normal stress differences and beyond-Navier-Stokes hydrodynamics. *Powders and Grains* (2017).
 - [27] R. Jackson, *Dynamics of Fluidized Particles* (Cambridge University Press, Cambridge, 2000).

- [28] E. Liss, S. Conway, and B. J. Glasser, Density waves in gravity-driven granular flow through a channel, *Phys. Fluids* **14**, 3309 (2002).
- [29] M. Tij and A. Santos, Poiseuille flow in a heated granular gas, *J. Stat. Phys.* **117**, 901 (2004).
- [30] K. C. Vijayakumar and M. Alam, Velocity distribution and the effect of wall roughness in granular Poiseuille flow, *Phys. Rev. E* **75**, 051306 (2007).
- [31] V. Chikkadi and M. Alam, Slip velocity and stresses in granular Poiseuille flow via event-driven simulations, *Phys. Rev. E* **80**, 021303 (2009).
- [32] M. Alam, V. Chikkadi, and V. Gupta, Density waves and the effect of wall roughness in granular Poiseuille flow: Simulation and linear stability, *Eur. Phys. J. Special Topics* **179**, 69 (2009).
- [33] M. Alam and V. Chikkadi, Velocity distribution function and correlations in granular Poiseuille flow, *J. Fluid Mech.* **653**, 175 (2010).
- [34] M. Alam, A. Mahajan, and D. Shivanna, On Knudsen-minimum effect and temperature-bimodality in dilute granular Poiseuille flow, *J. Fluid Mech.* **782**, 99 (2015).
- [35] R. Tehver, F. Toigo, J. Koplik, and J. R. Banavar, Thermal walls in computer simulation, *Phys. Rev. E* **57**, R17 (1998).
- [36] N. Khalil, V. Garzo, and A. Santos, Hydrodynamic Burnett equations for inelastic Maxwell models of granular gases, *Phys. Rev. E* **89**, 052201 (2014).
- [37] G. A. Bird, *Molecular Gas Dynamics and the Direct Simulation Monte Carlo of Gas Flows* (Clarendon, Oxford, 1994).
- [38] T. Pöschel and T. Schwager, *Computational Granular Dynamics* (Springer, Berlin, 2005).
- [39] L. Wu, H. Liu, J. M. Reese, and Y. Zhang, Nonequilibrium dynamics of dense gas under tight confinement, *J. Fluid Mech.* **794**, 252 (2016).
- [40] M. Alam and S. Luding, First normal stress difference and crystallization in a dense sheared granular fluid, *Phys. Fluids* **15**, 2298 (2003).
- [41] M. Alam and S. Luding, Rheology of bidisperse granular mixtures via event-driven simulations, *J. Fluid Mech.* **476**, 69 (2003).
- [42] M. Alam and S. Luding, Energy nonequipartition, rheology, and microstructure in sheared bidisperse granular mixtures, *Phys. Fluids* **17**, 063303 (2005).
- [43] M. Alam and S. Luding, Non-Newtonian granular fluid: Simulation and theory. In *Powders and Grains*, edited by R. Garcia-Rojo, H. J. Herrmann, and S. McNamara (Balkema, The Netherlands, 2005), pp. 1141–1145.